FIRST-PRINCIPLES DENSITY FUNCTIONAL THEORY STUDY TO AID UNDERSTANDING OF THE EFFECTS OF DOPING-INDUCED DEFECTS IN MATERIALS USED FOR SOLID OXIDE FUEL CELLS

by

Hepeng Ding

A dissertation submitted to the faculty of
The University of Utah
in partial fulfillment of the requirements for the degree of

Doctor of Philosophy

Department of Materials Science and Engineering

The University of Utah

August 2014

The University of Utah Graduate School

STATEMENT OF DISSERTATION APPROVAL

The following faculty members served as the supervisory committee chair and members for the dissertation of **Hepeng Ding**.

Dates at right indicate the members' approval of the dissertation.

Feng Liu, Chair	**04/01/2014** Date Approved
Anil V. Virkar, Member	**04/01/2014** Date Approved
Ling Zang, Member	**04/02/2014** Date Approved
Michael Scarpulla, Member	**04/02/2014** Date Approved
Zhigang Zak Fang, Member	_____ Date Approved

The dissertation has also been approved by **Feng Liu**

Chair of the Department/School/College of **Materials Science and Engineering**

and by David B. Kieda, Dean of The Graduate School.

ABSTRACT

The focus of this dissertation is to obtain an atomic-level understanding of the effects of doping-induced defects in materials used for solid oxide fuel cells (SOFCs), based on first-principles density functional theory (DFT) calculations. To improve the SOFC performance, doping technique is commonly adopted to introduce external defects, such as creating extra oxygen vacancies to speed up the ion conducting rate. Much experimental effort has been made to gain important fundamental understanding of defect properties in the SOFC materials, especially at the macroscopic level. On the other hand, computational studies can be useful to give microscopic views of defects at the atomic level, which are usually difficult to acquire from experiments. These computational studies can not only help explain experimental results, but also make predictive suggestions for new experiments. Based on first-principles DFT calculations, we have carried out a focused study of the effects of doping-induced defects in some SOFC related materials. Specifically, this dissertation includes three topics of studies: (1) defect configuration and phase stability of cubic vs. tetragonal yttria-stabilized zirconia; (2) suppression of Sr surface segregation in $La_{1-x}Sr_xCo_{1-y}Fe_yO_{3-\delta}$; (3) understanding cation ordering and oxygen vacancy site preference in $Ba_3CaNb_2O_9$. Overall, my dissertation demonstrates that DFT can be employed to aid our fundamental understanding of the effects of doping-induced defects on some key material properties governing the efficiency of SOFCs, and hence to benefit to the development of better SOFC materials.

TABLE OF CONTENTS

LIST OF TABLES

LIST OF FIGURES

ACKNOWLEDGEMENTS

I would like to express my sincerest appreciation to my advisor, Prof. Feng Liu, for his invaluable guidance and help throughout my graduate study. His incredible patience, amazing motivation, insightful advices, and broad knowledge make the whole learning process far more effective and full of joy. I would like to extend my deepest gratitude to my co-advisor, Prof. Anil V. Virkar, his rigorous attitude of scholarship, profound knowledge and persistent support is essential to this dissertation. I must be very lucky that I could have two of the most brilliant people I know as my advisors.

I am truly thankful to my external collaborators, Dr. Siwei Wang and Prof. Fanglin Chen from U. South Carolina, and especially thanks to Prof. Meilin Liu from Georgia Tech for his intuitive inspiring ideas and very important support. I am also very grateful to the other three committee members, Prof. Michael A. Scarpulla, Prof. Ling Zang, and Prof. Zhigang Zak Fang for their insightful scientific comments and helpful suggestions.

I also thank all the present and some of the past group members (Dr. Hao Hu, Dr. Miao Liu, Dr. Xiaobin Niu, Dr. Rujie Sun, et al.). Thanks to all the people for building up a friendly and pleasant working environment, and thanks for providing unfading support and friendship both in career and life.

I also thank the funding support from DOE HeteroFoam EFRC for the past five years. I benefited a lot from the center.

I especially thank my parents and sister for their unconditional love and care.

CHAPTER 1

BRIEF INTRODUCTION TO SOLID OXIDE FUEL CELLS AND DENSITY FUNCTIONAL THEORY

1.1 Introduction

A solid oxide fuel cell (SOFC) is an electrochemical conversion device that directly converts the chemical energy into electrical energy from oxidizing certain fuel[1]. The ability to overcome the Carnot cycle combustion efficiency limitation[2], along with the capability to oxidize any fuels in principle, along with the long-term stability and relatively low cost make SOFCs a promising technique for sustainable energy generations. To improve SOFC performance, reduction of overpotential, which is mainly produced from ions conducting through electrolytes and electrochemical activation barriers at the electrodes, is critical. Since substitutional doping can change the defect concentration and defect atomic configuration in electrolyte and electrode materials, it plays a significant role in tuning the overpotential. Thus, a comprehensive understanding of the effect of doping-induced defects on key material properties of electrolyte and electrode materials is critical to improve cell performance. Density functional theory (DFT) is among the most popular and the most successful quantum mechanical modeling approaches that can simulate the behavior of many materials accurately to better understand the experimental results, as well as to guide the experimental work by

predicting new materials properties. Therefore, the focus of this dissertation is to investigate the effect of doping-induced defects in SOFC materials using the DFT method. These include the defect configurations in the oxygen ion conducting electrolyte materials, defect induced variation of surface composition in cathode materials, and the origin of the ion ordering and defect formation site preference in the proton conducting electrolyte materials. In the following, we first give a brief introduction to SOFCs, followed by an overview to the history of DFT, and then provide a simple review of some of the applications of DFT calculations on the effects of defects in materials related to SOFCs, and lastly outline the dissertation organization.

1.2 Solid Oxide Fuel Cells

A SOFC unit cell consists of a three-layer membrane structure, including the anode, electrolyte and cathode; all of which are made of solid-state materials. The SOFC operates at high temperature in the range of 800-1000 ^{o}C for oxygen ion conducting SOFC or at intermediate temperature in the range of 500-700 ^{o}C for proton conducting SOFC[1], because generally protons migrate with much lower activation energy for proton migration than oxygen ion[3]. Unit cells are stacked together to be used as a single cell which achieves the desired output voltage and power.

Figure 1.1(a) and Figure 1.1(b) show the schematics of the conventional oxygen ion conducting unit fuel cell and the proton conducting unit fuel cell with the simplest setup where a fuel cell operates with pure hydrogen and oxygen, respectively. In the conventional oxygen ion conducting SOFC, the oxygen gas is introduced to the cathode side, where the oxygen reduction reaction occurs, decomposing the O_2 molecule to O^{-2}, and then the O^{-2} is transported to the anode side through the oxygen ion conducting

electrolyte. The hydrogen gas is introduced to the anode side, that reacts with the O^{-2}, outputting H_2O at the cathode side and generating electrons that flow through an external electrical circuit to create a direct current and power a load. In the proton conducting SOFC, the hydrogen gas is introduced to the anode side, where each hydrogen molecule is catalyzed into H^+ plus two electrons. The produced electrons flow through an external electrical circuit to generate a direct current and power a load. Meanwhile, the H^+ is transported to the cathode side through the proton conducting electrolyte. Hydrogen gas is introduced to the anode side, which reacts with the O_2 and outputs H_2O at the anode side.

The materials commonly used in the oxygen ion conducting SOFCs are $LaMnO_3/La_{1-x}Sr_xMnO_{3-\delta}$ (LSM)/$La_{1-x}Sr_xCo_{1-y}Fe_yO_{3-\delta}$ (LSCF), yttria-stabilized zirconia (YSZ)/yttria-doped ceria, and Ni+YSZ, for cathode, electrolyte, and anode, respectively[4]. The commonly used materials in the proton conducting SOFCs are porous Pt/Ag/cobaltate, doped $SrCeO_3/BaCeO_3/BaCe_{1-x}Ln_xO_{3-\delta}/Ba_3Ca_{1+x}Nb_{2-x}O_{9-\delta}$ (BCN), and porous Pt/Ni, for cathode, electrolyte, and anode, respectively[3]. The anode and cathode are places where half chemical reactions take place, and the electrolyte serves two roles: an ionic conductor and a physical separation to prevent direct mixing of fuel and oxygen. As long as the fuel and oxygen are continuously supplied, the fuel cell continues to operate at a steady power output with the Nernst potential determined by the concentration gradient across the fuel cell[5].

Since the SOFCs are mainly based on ceramics and metals as electrodes, they exhibit important advantages, including the ability to withstand significantly higher temperature, no external fuel reforming, flexibility with any gaseous fuel, long-term operation,

variable cell shapes, inexpensive catalyst, colossal alleviation of corrosion problems as encountered with liquid electrolytes[5], scalable output power, and high energy conversion efficiency. Therefore, SOFCs are receiving an increasing amount of attention both in academic research and industrial applications. The main remaining challenges include lowering the high operating temperature, improving chemical and mechanical durability, and mitigating carbon cracking[6].

1.3 Density Functional Theory

Owing to the considerable systematic improvement in computing power (hardware) and computational algorithms (e.g., parallel algorithm), the usage of computational modeling and simulation methods are more and more accepted as complementary studies to experiments and become essential to understanding properties that cannot be directly probed by experiments. From standard quantum mechanics, it is well known that the many-body Schrödinger equation underlies all materials' properties, but its exact or analytical solutions are usually impractical to obtain. Based on the Born-Oppenheimer[7] approximation, the solution becomes much easier because this approximation decouples the dynamics of electrons from that of nuclei. However, computation of electronic energy and wave function is still very difficult and time consuming. To further simplify the problem, Hohenberg and Kohn[8] proved two well-known theorems as the foundation of DFT: one is the ground state electron density, which determines the potential of a system; and the second one is using the electron density as the variational quantity instead of the electron wave function. Following Hohenberg-Kohn theory, instead of directly solving the Schrödinger equation (Eq. 1.1),

$$\hat{H}\Psi(r_1, r_2, \ldots, r_N) = E\Psi(r_1, r_2, \ldots, r_N) \quad (1.1)$$

The total potential energy functional of a system can be written as Eq. 1.2[8],

$$E[\rho] = T[\rho] + V_{ext}[\rho] + V_{ee}[\rho] \quad (1.2)$$

Here, $\hat{H}$ is the Hamilton operator, Ψ is the wave function of the quantum system, r_i is the coordinate of electron i (i ranges from 1 to N), E is energy of state Ψ, ρ is the electron density, T is the kinetic energy, V_{ext} is the potential energy from the external field due to positively charged nuclei, and V_{ee} is the electron-electron interaction energy. In Eq. 1.2, the kinetic energy functional and the electron-electron interaction energy functional are unknown. To perform minimization of the total energy, good approximations to the above two functionals are essential.

Kohn and Sham[8] proposed that the ground state density of a fully interacting many-body system is equal to that of a fictitious system of N noninteracting system where the electrons do not interact, in which the kinetic energy and electron density are known exactly from the set of orbitals. This assumption replaces the original many-body problem by an independent electron problem that can be solved where only the ground-state density and the ground-state energy are required to be the same as in the original many-body system. In addition, we also note that the classical coulomb interaction is dominated by the electron-electron interaction which is commonly referred as Hartree energy ($V_{Hartree}$). Then the energy functional of Eq. 1.2 can be further written in Kohn-Sham approach, becoming Eq. 1.3,

$$E[\rho] = T_s[\rho] + V_{ext}[\rho] + V_{Hartree}[\rho] + E_{xc}[\rho] \quad (1.3)$$

Here, $T_s[\rho]$ notation highlights that this is not the true kinetic energy of the many-body system but is that of a system of noninteracting electrons. The $E_{xc}[\rho]$ term can be expressed as Eq. 1.4,

$$E_{xc}[\rho] = (T[\rho] - T_s[\rho]) + (V_{ee}[\rho] - V_{Hartree}[\rho]) \quad (1.4)$$

In Eq. 1.3, we have introduced the exchange-correlation functional E_{xc}, which incorporates both the exchange and correlation energies, as well as anything that might be missing in order for the energy functional $E(\rho)$ to be the true energy functional from Eq. 1.2 (e.g., the errors induced by treating the electron-electron interaction classically, and by using a noninteracting kinetic energy). Thus far, E_{xc} is the only remaining term which cannot be written as a closed mathematical expression.

Fortunately, a useful universal functional for E_{xc} can be approximated. The simplest form is developed by Kohn and Sham, which is called local-density approximation (LDA) [9]. This functional calculates the E_{xc} solely depending on the value of the electron density at each point in a system to be the same as that of a point in a homogenous electron gas of the same density. Material properties such as lattice parameters, electronic structure, elastic properties, phase stability, and vibrational frequencies are successfully described across many systems. The success of LDA demonstrates that these simple approximations to the exchange-correlation functional can provide very good results. LDA serves as an important basis in the construction of more complex approximations, such as generalized gradient approximations[10] which take into account the gradient of the density at the same coordinate, or hybrid functional[11] which mixes in the exact exchange energy from the Hartree-Fock theory[12].

Over many years of development, DFT has become one of the most popular and successful *ab initio* quantum mechanical methods for predicting or studying various properties of a wide range of different materials. These include structural properties, such as lattice parameters and atomic coordination; lattice dynamics, such as phonon frequencies and vibrational entropy; electronic structures, such as band structure, electron density of states, and electric field gradients; and spectroscopies, such as electron energy loss.

1.4 DFT Study of SOFC Materials

Although it is not practical today to directly simulate the whole SOFC system using *ab initio* methods, some critical aspects can be accurately treated, such as the studies of the effects of doping-induced defects, as have been performed in the past. For example, Carter and her coworkers[13] performed a quantum mechanical analysis of formation of oxygen vacancies in $LaMO_3$ (M denotes Cr, Mn, Fe, Co) materials, providing a basis for design principles for SOFC cathode materials from easily measurable or computable properties. Morgan and his coworkers[14] demonstrated *ab initio* energetics and empirical modeling can be combined to develop a defect model for $LaMnO_3$ that predicts defect concentrations, agreeing well with experimental results. Maier and his coworkers[15] identified the most probable reaction mechanism for oxygen incorporation into LSM cathode materials using DFT calculations, found a correlation between the reaction preferred mechanism and point defect concentrations. Ceder and his coworkers[16] predicted the ordered ground-state structures in YSZ using *ab initio* search, proposing that a short-range order may occur at nonzero temperatures. Vanderbilt and his coworkers[17] found the compositional inversion symmetry breaking in the ferroelectric

complex perovskite oxides due to isovalent/heterovalent substitution, proposing the basis for the allowance of optimization of desired materials properties. Asta and his coworkers[18] performed a first principles study on the dopant-defect interactions in proton conductor Sr-doped $LaPO_4$, showing that dopant binding stabilizes the proton incorporation, lowering the proton transport kinetic rate. These studies are suggestive of the effectiveness of the *ab initio* defect energetics in describing the defect chemistry in complex oxides.

Once the DFT model setup is validated, due to its inherent parameter-free nature, it is rather reliable in providing accurate prediction of materials' properties, providing fundamental understanding of material properties at the atomic-level. DFT calculations are particularly valuable in situations when experimental observations are difficult or cannot be probed directly. In order to treat the material properties of interest more correctly, DFT+U[19] method are sometimes used since many materials used in SOFCs are referred to as strongly correlated classes of materials, having transition metal ions with open shell 3*d* or 4*f* electrons. The main difference between DFT and DFT+U lies in that the electrons are separated into two subsystems: localized *d* or *f* electrons for which the spurious intra-atomic self-Coulomb repulsion is cancelled by taking into account of the exact intra-atomic HF exchange; and the rest of the electrons are described using the one-electron potential within DFT as always.

1.5 Dissertation Organization

The remaining chapters of this dissertation are divided into three chapters and are arranged as follows. In Chapter 2, study on "defect configuration and phase stability of cubic vs. tetragonal yttria-stabilized zirconia" [20] is presented. Using first-principles

calculations, we have carried out a systematic comparative study of the microscopic atomic defect configurations in cubic and tetragonal YSZ and their correlation with the macroscopic lattice parameters and relative phase stability, as a function of Y concentration. We found Y atoms sit at the second-nearest-neighbor cation sites to oxygen vacancies and repel each other; oxygen vacancies form pairs and these pairs repel each other. Using the optimized defect configurations as inputs, we correctly identify the experimentally observed tetragonal to cubic transition point and predict the changes of lattice parameters with the increasing Y concentration, in excellent agreement with experiment. Our studies reveal an interesting correlation between the microscopic atomic defect configuration and macroscopic lattice properties.

In Chapter 3, our focus is on the topic of "suppression of Sr surface segregation in $La_{1-x}Sr_xCo_{1-y}Fe_yO_{3-\delta}$: a first-principles study" [21]. Based on systematic first principles calculations, we investigate Sr surface segregation (SSS) in LSCF (a typical perovskite ABO_3 compound), a bottleneck causing efficiency degradation of solid oxide fuel cells. We identify two basic thermodynamic driving forces for SSS and suggest two possible ways to suppress SSS: applying compressive strain and reducing surface charge. We show that compressive strain can be applied through doping of larger elements and surface coating; surface charge can be reduced through doping of higher-valence elements in the Sr- and B-site or lower-valence elements in the La-site and introducing surface A-site vacancies. The net effect of oxygen vacancy is to enhance SSS because its effect of increasing surface charge overrides its effect of inducing compressive strain, while Co substitution of Fe always enhances SSS because it induces tensile strain as well as increases surface charge. Our results explain the recent experimental observation of

SSS suppression in LSCF by a $La_{1-x}Sr_xMnO_{3-\delta}$ **(**LSM) coating.

In Chapter 4, the topic of "understanding cation ordering and oxygen vacancy site preference in $Ba_3CaNb_2O_9$ from first-principles study" [22] is presented. Using DFT calculations, we investigate the physical mechanism underlying the formation of the B-site cation ordering and the oxygen vacancy site selection in BCN. We found that either cation site exchange or oxygen vacancy formation induces negligible lattice strain. This implies that the ionic radius plays an insignificant role in governing these two processes. Furthermore, the electrostatic interactions are found dominant in the ordering of mixed valence species on one or more sites, the ionic bond strength is identified as the dominant force in governing both the 1:2 B-site cation ordering along the <111> direction and the oxygen vacancy site preference in BCN. Specifically, the cation ordering can be rationalized by the increased mixing bonding energy of the Ca-O-Nb bonds over the Ca-O-Ca and Nb-O-Nb bonds, i.e., 1/2(Ca-O-Ca + Nb-O-Nb) < Ca-O-Nb; while oxygen vacancy prefers a site to minimize the electrostatic energy and to break the weaker B-O-B bond.

1.6 References

[1] N. Tikekar, T. Armstrong, and A. Virkar, *ECS Proceedings* **26**, 81 (2002).

[2] S.C. Singhal, *Solid State Ionics* **135**, 305 (2000).

[3] K.D. Kreuer, Annu. *Rev. Mater. Res.* **33**, 333 (2003).

[4] A. Virkar, J. Chen, C. Tanner, and J. Kim, *Solid State Ionics* **131**, 189 (2000).

[5] S. Singhai, *Solid State Ionics* **135**, 305 (2000).

[6] A. Dicks, *J. Power Sources* **71**, 111 (1998).

[7] M. Born, and J. Oppenheimer, *Annalen der Physik* **389**, 457 (1927).

[8] P. Hohenberg, and W. Kohn, *Phys. Rev.* **136**, B864 (1964).

[9] W. Kohn, and J. Sham, *Phys. Rev.* **140**, A1133 (1965).

[10] J. Perdew, K. Burke, and M. Ernzerhof, *Phys. Rev. Lett.* **77**, 3865 (1995).

[11] A. Becke, *J. Chem. Phys.* **98**, 1372 (1993).

[12] J. Slater, *Phys. Rev.* **81**, 385 (1951).

[13] M. Pavone, A. Ritzmann, and E. Carter, *Energy Environ. Sci.* **4**, 4933 (2011).

[14] Y. Lee, and D. Morgan, *Phys. Chem. Chem. Phys.* **14**, 290 (2012).

[15] Y. Mastrikov, R. Merkle, E. Heifets, E. Kotomin, and J. Maier, *J. Phys. Chem. C* **114**, 3017 (2010).

[16] A. Predith, G. Ceder, C. Wolverton, K. Persson, and T. Mueller, *Phys. Rev. B* **77**, 144104 (2008).

[17] N. Sai, B. Meyer, and D. Vanderbilt, *Phys. Rev. B* **84**, 5636 (2000).

[18] J. Solomon, N. Adelstein, L. Jonghe, and M. Asta, *J. Mater. Chem. A* **2**, 1047 (2014).

[19] V. Anisimov, F. Aryasetiawan, and A. Liechtenstein, *J. Phys.: Condens. Matter* **9**, 767 (1997).

[20] H. Ding, A. Virkar, and F. Liu, *Solid State Ionics* **215**, 16 (2012).

[21] H. Ding, A. Virkar, M. Liu and F. Liu, *Phys. Chem. Chem. Phys.* **15**, 489 (2013).

[22] H. Ding, A. Virkar, and F. Liu, *Bulletin of APS* **59**, 1 (2014).

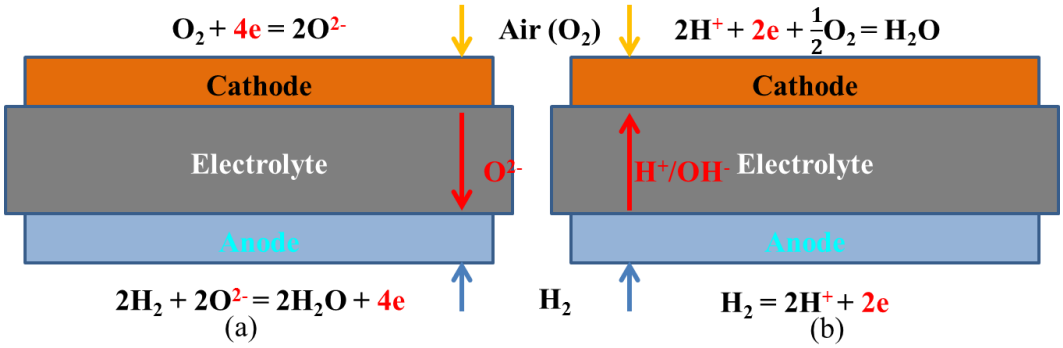

Fig. 1.1 Schematic diagram of a SOFC unit cell. (a) Conventional oxygen ion conducting SOFC; (b) Proton conducting SOFC.

CHAPTER 2

DEFECT CONFIGURATION AND PHASE STABILITY OF CUBIC VERSUS TETRAGONAL YTTRIA-STABILIZED ZIRCONIA

2.1 Introduction

YSZ is the most commonly used electrolyte in solid oxide fuel cells (SOFC) for its high ionic and low electronic conductivity. Pure zirconia displays a monoclinic structure ($P2_1/c$) up to a temperature of around 1400 K[1], where monoclinic to tetragonal ($P4_2/nmc$) transition occurs. The cubic ($Fm3m$) phase exists at temperatures higher than 2600 K[2]. The addition of yttria introduces oxygen vacancies for charge compensation, and stabilizes the tetragonal and cubic phases at low temperatures[3,4]. Although the ionic conductivity of YSZ is attributed to the presence of oxygen vacancies introduced by Y doping, it does not simply increase monotonically with the increasing Y concentration but instead displays a maximum at the 15%-18% Y concentration[5]. This interesting behavior of ionic conductivity is ascribed to the change of atomic configurations of YSZ as a function of Y concentration. In particular, two possible reasons are identified: (1) too high an oxygen vacancy concentration leads to formation of high activation energy pathways for oxygen diffusion[6,7], and (2) formation of ordered oxygen vacancy complexes at high Y concentrations hinders the vacancy mobility[8]. It has become evident that the atomic defect configuration of Y and oxygen vacancy complexes have a

profound effect on the oxygen diffusion and transport in YSZ, and hence on the efficiency of SOFC. Furthermore, the defect configuration is expected to be correlated with the phase stability of different YSZ phases, especially the cubic and tetragonal phases stabilized upon Y doping. Therefore, a detailed study of the defect configuration and phase stability of cubic vs. tetragonal YSZ, as a function of Y concentration, is of both fundamental interest and technological significance.

A great deal of theoretical and experimental work has been dedicated to the defect interactions in cubic YSZ and some work has also been done with respect to the defect configuration in tetragonal YSZ. However, there exist quite some discrepancies in the literature. When Y_2O_3 is added to ZrO_2, for every two Y atoms replacing two Zr atoms, one oxygen vacancy is created to satisfy charge compensation. Most previous studies found that the oxygen vacancies occupy positions as the second nearest neighbors (2NNs) to the two Y atoms and next to Zr atoms in both cubic and tetragonal YSZ[9-17]. Other studies suggested that the oxygen vacancies prefer to be the NNs[18-22] or 3NNs to the Y atoms[23], or change their preferred sites with changing Y concentration[24]. For high Y doping concentrations, some studies found that Y atoms repel each other in cubic YSZ[9] while others suggested attraction between Y[15,23], and Y-Y interaction was suggested to be attractive in tetragonal YSZ[17]. Oxygen vacancies are found to have a tendency to form pairs in cubic YSZ, with a variety of pairing directions suggested, such as <1 0 0>[25], <$\frac{3}{2}\frac{1}{2}$ 0>[25], <1 1 1>[8,14,23,26-28], <1 1 2>[29], and <1 $\frac{1}{2}$ 0>[30]. One study showed that in tetragonal YSZ, oxygen vacancies repel each other, staying as far as possible[17]. Several papers studied the oxygen pair interactions in cubic YSZ and suggested different alignment directions, such as <1 1 2>[8,29] and <1 $\frac{1}{2}$ 0>[14].

In the present study, we revisit the problem of atomic defect configurations in both cubic and tetragonal YSZ. Using extensive first-principles calculations, we examine all the possible defect-defect interactions as a function of Y, including Y-$V_{\ddot{O}}$ (oxygen vacancy), Y-Y, $V_{\ddot{O}}$-$V_{\ddot{O}}$, and $V_{\ddot{O}}V_{\ddot{O}}$ pair-$V_{\ddot{O}}V_{\ddot{O}}$ pair interactions, to identify the most energetically favorable defect configuration. Furthermore, as an independent check of our results, we use the optimized defect configurations as inputs to calculate the relative phase stability of cubic and tetragonal YSZ and their lattice parameters as a function of Y concentration, to facilitate a direct comparison with experiments. We are able to predict the tetragonal to cubic phase transition point with Y doping and the trends of changing lattice parameters of both phases as the Y concentration increases. Our results are in very good agreement with the experiments, which in turn confirms the correctness of the defect configurations we found. Furthermore, our studies reveal an interesting correlation between the microscopic atomic defect configuration and macroscopic lattice properties.

2.2 Computational Method

All the calculations are performed using the FHI-aims[31], an ab initio density-functional theory (DFT) code employing all electron basis sets. An fcc-like unit cell containing 4 ZrO_2 formulas and a $2\times2\times2$ fcc-like supercell containing 32 ZrO_2 base formulas are used for modeling ZrO_2 and YSZ, respectively. The energy cutoff and the force criterion used are 10^{-6} eV and 10^{-4} eV/Å, respectively. To ensure convergence, light basis settings for Zr, Y, and additional 4f orbital of tier2[32] added O, along with a 768 k-point×atom mesh are used to give lattice constant variances smaller than 10^{-2} Å and relative phase energy difference variances smaller than 5 meV/formula. For exchange and correlation functional, PW-LDA[33] formula is used. According to our calculation results, it

gives better agreement with the experiment[37, 38] in terms of relative phase stability for cubic, tetragonal, and monoclinic phases than PBE[34] formula.

2.3 Results and Discussion

2.3.1 Lattice and Structural Properties of ZrO_2

As a benchmark of our methods, we first calculated the structural and energetic properties of three pure ZrO_2 phases. For cubic ZrO_2, only one lattice parameter, the lattice constant *a* needs to be optimized, since all the atoms sit in the high-symmetry points of the fcc lattice sites. For tetragonal ZrO_2, two lattice parameters, *a* and *c*, and one internal atomic coordinate, the *z*-component of O atom, need to be optimized, since the O is displaced from the high-symmetry lattice point along the z-axis by Δz or in unit of lattice parameter *c* as $dz = \Delta z/c$. For monoclinic ZrO_2, four lattice parameters, *a*, *b*, *c* and β (β is the angle between x and z axils), and nine internal atomic coordinates need to be optimized, since there are three kinds of atoms all without any symmetry constraint.

Our optimized lowest-energy lattice and structural properties are shown in Table 2.1, along with the available experimental data and several previous calculation results for comparison. The monoclinic structure is the most stable phase at absolute zero temperature and the specific volume per ZrO_2 formula follows the order of $V_{cubic} < V_{tetragonal} < V_{monoclinic}$. In general, our results are in good agreement with the experimental and previous computational results, which validates the method we use.

2.3.2 Defect Configurations in Cubic and Tetragonal YSZ

As Y is doped to substitute Zr in ZrO_2 and accompanied with oxygen vacancies to form YSZ, three basic kinds of defect interactions are introduced, namely, $V_{\ddot{O}}$-Y, Y-Y

and $V_{\ddot{O}}$–$V_{\ddot{O}}$ interactions. To find the most stable defect configuration in YSZ, all three interactions need to be examined for energy minimization, and the results are expected to sensitively depend on Y concentration because these interactions shall change with the changing Y concentration. Furthermore, possible change of lattice structure needs also to be considered, because the relative stability of different phases, e.g., cubic and tetragonal phases, depends on the internal structure of defect configurations. We have carried out a systematic comparative study of defect configurations in cubic and tetragonal YSZ by calculating all three kinds of defect interactions to determine the most stable defect configurations as a function of Y concentration. Using the optimized lowest-energy defect configuration as inputs, we further validate the results by predicting the Y doping induced phase transition between the cubic and tetragonal phases and changes of lattice parameters with Y concentration, in comparison with the available experimental results.

In what follows, if not specified, the energy is presented as the relative energy in unit of eV/supercell, with the lowest-energy configuration set as the reference of zero energy. For convenience, the notation of [*a*,*b*,*c*] or <*a*,*b*,*c*> is used to denote not only the direction but also the separation distance along the given lattice axis.

2.3.2.1 Defect Interactions in Cubic YSZ

2.3.2.1.1 Defect configuration of one basic doping unit: $V_{\ddot{O}}$-Y and Y-Y interactions. Since one oxygen vacancy is created to accompany two doped Y atoms, one considers a Y-$V_{\ddot{O}}$-Y trimer as the most basic doping unit, whose configuration, involving both $V_{\ddot{O}}$-Y and Y-Y interactions, is to be determined first. To study the configuration of one single Y-$V_{\ddot{O}}$-Y trimer unit, which is the dominating configuration at low Y concentration limit, we introduce one oxygen vacancy and two Y atoms in the supercell, as shown in Fig. 2.1.

First, we examined the $V_{\ddot{O}}$-Y interactions by changing the distances of two Y atoms from the oxygen vacancy. Around an oxygen vacancy, there are four NN, twelve 2NN and twelve 3NN Zr sites for the two Y atoms to occupy. The relative energies of different occupations are calculated as shown in Table 2.2. We found that the most stable Y-$V_{\ddot{O}}$-Y trimer configuration is to have both Y atoms sitting at the 2NN positions to the oxygen vacancy, denoted as the 2NN/2NN configuration in Table 2.2. The NN/3NN configuration, i.e., with one Y being the NN and the other Y being the 3NN to the oxygen vacancy, has the second lowest energy. Our results agree with the majority of previous experimental and theoretical studies[9-16], but disagree with some other studies showing the NN/NN[18-22] or 3NN/3NN[23] to be the lowest-energy configuration.

We believe that the 2NN/2NN preference is due to the balance between electrostatic energy (Y^{3+} vs. Zr^{4+}) and strain energy (the ionic radius r(Y^{3+}) =1.04 nm[38] is larger than r(Zr^{4+}) = 0.86 nm[38]). In view of the electrostatic energy, Y^{3+} instead of Zr^{4+} prefers to stay close to oxygen vacancy to reduce Coulomb energy because oxygen vacancy has a positive effective charge. However, in view of the ionic radius, Y^{3+} prefers to have more room for its larger size. "Structural relaxation" shows that a cation next to the oxygen vacancy, surrounded by seven oxygen atoms, will have smaller room than a normal cation site, surrounded by eight oxygen atoms without oxygen vacancy. Consequently, Y^{3+} prefers to stay away from the oxygen vacancy to reduce strain energy. Thus, the competition of these two energies results in the Y atoms sitting at the 2NN cation sites of oxygen vacancy.

Among the twelve 2NN cation sites to oxygen vacancy, which are all equivalent in cubic YSZ, the two Y atoms may also arrange differently to minimize the Y-Y

interaction. There are three choices in terms of Y-Y separation, which we denoted in the ascending order of separation as YY-1, YY-2 and YY-3 in Table 2.2. Clearly, due to Coulomb repulsion, the Y-Y interaction energy decreases with the increasing Y-Y separation, as shown in Table 2.2. This agrees with Stapper et al.[8] but disagrees with Bogicevia et al.[23] who suggested that Y-Y was attractive with each other favoring the YY-1 positions. Also to be noted is that the $V_{\ddot{O}}$-Y interaction energies shown in Table 2.2 as discussed above are results with the minimum Y-Y interaction energy or the largest Y-Y separation for any given $V_{\ddot{O}}$-Y separation. Thus, to minimize both $V_{\ddot{O}}$-Y and Y-Y interactions, the most stable defect configuration of a Y-$V_{\ddot{O}}$-Y trimer, the basic doping unit of Y_2O_3 in ZrO_2, is to have two Y atoms occupying the 2NN cation sites to the oxygen vacancy with the greatest Y-Y separation, as shown in Fig. 2.1(a).

2.3.2.1.2 Defect configuration of two doping units: $V_{\ddot{O}}$-$V_{\ddot{O}}$ interaction. As more Y_2O_3 is added to ZrO_2, the distribution of the basic doping unit, Y-$V_{\ddot{O}}$-Y trimer, defines the defect configuration, which is determined by the interactions between the doping units. Keeping the basic Y-$V_{\ddot{O}}$-Y trimer configuration intact, their interactions can be effectively characterized by the $V_{\ddot{O}}$-$V_{\ddot{O}}$ interaction. To study the $V_{\ddot{O}}$-$V_{\ddot{O}}$ interaction, we introduce two oxygen vacancies and four Y atoms into the supercell, which corresponds to a 12.5% Y concentration. Within the supercell, there are nine choices of O vacancy separations along different crystallographic directions, denoted as <$\frac{1}{2}$,0,0>, <$\frac{1}{2}$, $\frac{1}{2}$,0>, <$\frac{1}{2}$, $\frac{1}{2}$, $\frac{1}{2}$>, <1,0,0>, <1, $\frac{1}{2}$,0>, <1, $\frac{1}{2}$, $\frac{1}{2}$>, <1,1,0>, <1,1, $\frac{1}{2}$ >, and <1,1,1> having a separation distance equal to 0.5*a*, 0.707*a*, 0.866*a*, *a*, 1.118*a*, 1.225*a*, 1.414*a*, 1.5*a*, and 1.732*a*, respectively, where a = 5.031Å is the lattice constant. The relative energies of these nine $V_{\ddot{O}}$-$V_{\ddot{O}}$ separations are shown in Table 2.2 with the lowest energy separation <1,$\frac{1}{2}$,$\frac{1}{2}$> set as the

reference of zero energy. Interestingly, instead of being separated as far as possible, oxygen vacancies prefer to have the alignment of <1, $\frac{1}{2}$, $\frac{1}{2}$>. Another preferred alignment is <1,$\frac{1}{2}$,0> which has almost a degenerate energy with <1, $\frac{1}{2}$, $\frac{1}{2}$>. We consider these two lowest-energy alignments of oxygen vacancies as one $V_{\ddot{O}}V_{\ddot{O}}$ pair.

A large variety of experimental and computational results can be found in literature regarding the oxygen vacancy alignment. In experiments, Dai et al.[25] found that oxygen vacancies have an alignment along <1,0,0> or <$\frac{3}{2}$, $\frac{1}{2}$,0> direction, Osborn et al.[26] and Hull et al.[27] found that oxygen vacancies have an ordering along <$\frac{1}{2}$, $\frac{1}{2}$, $\frac{1}{2}$>, and Goff et al.[8] found that oxygen vacancies have an alignment along <1 1 1>. In theory, our results agree with Predith et al.[29] who found that oxygen vacancies form parallel <1 1 2> chains by using cluster expansion method combined with DFT. In contrast, Dalach[30] found that oxygen vacancies have a significant ordering along <1,$\frac{1}{2}$,0> also by using cluster expansion method. Several other papers reported different alignment directions using different computational methods. Bogicevia et al.[23,28] and Ostanin et al.[14] found that oxygen vacancy has an ordering along <$\frac{1}{2}$, $\frac{1}{2}$, $\frac{1}{2}$>, and Fabris et al.[40] found that the clustering of oxygen vacancies align along <1 1 1>.

2.3.2.1.3 Defect configuration of two doping unit pairs: $V_{\ddot{O}}V_{\ddot{O}}$ pair- $V_{\ddot{O}}V_{\ddot{O}}$ pair interaction. At even higher Y concentration, multiple interactions between doping units and unit pairs become very complicated. From Tables 2.2 and 2.3, we can see that the order of interaction strength goes like $V_{\ddot{O}}$-$V_{\ddot{O}}$ (~1.00 eV) > Y-$V_{\ddot{O}}$-Y (~0.50 eV) > Y-Y (~0.20 eV). Therefore, below we will focus on the $V_{\ddot{O}}$-$V_{\ddot{O}}$ interaction in the discussion of Y-$V_{\ddot{O}}$-Y trimer distribution. By treating the unit pair as a whole, we further attempted to

study defect configurations at the 25% Y concentration, in terms of $V_{\ddot{O}}V_{\ddot{O}}$ pair-$V_{\ddot{O}}V_{\ddot{O}}$ pair interaction, by introducing four oxygen vacancies and eight Y atoms into a supercell. We considered the pair-pair alignment and interaction in two ways. First, we set the lowest-energy oxygen vacancy pair of the <1, $\frac{1}{2}$, $\frac{1}{2}$> alignment as the basic interacting units denoted as case 1, and calculated the pair-pair interaction energies as a function of their separation direction and distance as listed in Table 2.2. We found that the <1, $\frac{1}{2}$, $\frac{1}{2}$> $V_{\ddot{O}}V_{\ddot{O}}$ pairs repel each other, with the interaction energy decreasing with the increasing separation. The system has the lowest energy when the two <1, $\frac{1}{2}$, $\frac{1}{2}$> $V_{\ddot{O}}V_{\ddot{O}}$ pair is separated by <0,1,1> which is the largest possible separation in our supercell. In the second case, we assume the <0,1,1> is the most favorable separation direction as found in case 1 between two oxygen vacancy pairs, and then determine the preferred the alignment of each oxygen pair. We found that at any separation distance along <0,1,1>, the lowest-energy alignment of $V_{\ddot{O}}V_{\ddot{O}}$ pair is the <1, $\frac{1}{2}$, $\frac{1}{2}$>. For example, the two <1,$\frac{1}{2}$,0> $V_{\ddot{O}}V_{\ddot{O}}$ pairs interaction energy is much higher than that of two <1, $\frac{1}{2}$, $\frac{1}{2}$> $V_{\ddot{O}}V_{\ddot{O}}$ pairs along the <0,1,1>, as shown in Table 2.2. The same results are also found for the 18.75% Y concentration with three oxygen vacancies and six Y atoms introduced in the supercell (not shown). This indicates that at high Y concentration, the <1, $\frac{1}{2}$, $\frac{1}{2}$> $V_{\ddot{O}}V_{\ddot{O}}$ pair alignment becomes the only dominant oxygen vacancy pair configuration, even though at low Y concentration the <1,$\frac{1}{2}$,0> alignment can be present too with almost degenerate energy with the <1, $\frac{1}{2}$, $\frac{1}{2}$> alignment. Such change of preferred $V_{\ddot{O}}V_{\ddot{O}}$ pair alignments with Y concentration may have an important effect on the relative phase stability and lattice

properties of cubic and tetragonal phases as a function of Y concentration as we will show below.

To summarize the defect interactions in cubic YSZ, the Y-$V_{\ddot{O}}$-Y trimer represents the basic doping unit with Y atoms sitting at the 2NN of oxygen vacancy and repelling each other among themselves; the Y-$V_{\ddot{O}}$-Y trimer units form pairs along the <1,$\frac{1}{2}$,0> and <1, $\frac{1}{2}$, $\frac{1}{2}$> at low Y concentration, while only the <1, $\frac{1}{2}$, $\frac{1}{2}$> alignment dominates at high Y concentration; the <1, $\frac{1}{2}$, $\frac{1}{2}$> $V_{\ddot{O}}V_{\ddot{O}}$ pairs align along <0,1,1> and repel each other. We may compare our results of the $V_{\ddot{O}}V_{\ddot{O}}$ pair interactions in cubic YSZ with previous studies. In experiments, Goff et al.[8] found that oxygen vacancy pairs pack together in <1 1 2> directions as Y concentration increases, which is consistent with our results of preferred <1, $\frac{1}{2}$, $\frac{1}{2}$> alignment. In theory, Predith et al.[29] also found that $V_{\ddot{O}}$-$V_{\ddot{O}}$ pairs order along the <1, $\frac{1}{2}$, $\frac{1}{2}$> direction.

2.3.2.2 Defect Interactions in Tetragonal YSZ

2.3.2.2.1 Defect configuration of a basic doping unit: $V_{\ddot{O}}$-Y and Y-Y interactions. In tetragonal YSZ, there exists a lattice asymmetry as the *c*-axis is larger than the *a*-axis and correspondingly the internal structure exhibits anisotropy in terms of oxygen atomic positions, i.e., the oxygen atoms are displaced along the *c*-axis making their z-coordinates distinguishable from x- and y-coordinates. Consequently, the positions of oxygen vacancies upon Y doping and hence, the defect configurations, have an isotropic preference in choosing the z-direction alignments from the alignments in the other two directions. Consider the basic doping unit of a Y-$V_{\ddot{O}}$-Y trimer, as found in the cubic YSZ, with two Y atoms sitting at the 2NN sites to an oxygen vacancy. In the tetragonal YSZ,

the twelve 2NN cation sites to the oxygen vacancy are no longer equivalent. As shown in Fig. 2.1(b), two 2NN cation sites have the smallest $V_{\ddot{O}}$-Y/Zr distance (denoted as 2NN-1), four 2NN cation sites have the second smallest $V_{\ddot{O}}$-Y/Zr distance (denoted as 2NN-2), another four 2NN cation sites have the second largest $V_{\ddot{O}}$-Y/Zr distance (denoted as 2NN-3), and two 2NN cation sites have the largest $V_{\ddot{O}}$-Y/Zr distance (denoted as 4). Among them, the two Y atoms may occupy different sites to minimize the repulsive Y-Y interaction, while at the same time to maximize the attractive $V_{\ddot{O}}$-Y interactions due to the slightly different 2NN $V_{\ddot{O}}$-Y distances. Our calculated relative configuration energies are shown in Table 2.3. Here, 11[YY-1] denotes both Y atoms sit at the 2NN-1 sites having the smallest $V_{\ddot{O}}$-Y distance while the separation between two Y atoms is YY-1, the smallest. The results in Table 2.3 indicate that the balance between the Y-Y repulsion and the $V_{\ddot{O}}$-Y attraction defines the lowest energy configuration. For the fixed Y-Y separation, the configuration with smaller $V_{\ddot{O}}$-Y separation is more preferred, for example, E (22 [YY-3]) < E (33 [YY-3]). For the fixed $V_{\ddot{O}}$-Y distance, the larger the Y-Y distance, the lower the configuration energy; for example, E (22 [YY-3]) < E (22 [YY-1]). Among all possibilities, the 13[YY-3] and the 11[YY-1] configurations (as shown in Fig. 2.1(b)) have the lowest energy. This finding is consistent with the previous work by Eichler[17].

2.3.2.2.2 Defect configuration of two doping units: $V_{\ddot{O}}$-$V_{\ddot{O}}$ interaction. Similar to the study of cubic YSZ discussed earlier, we introduce two oxygen vacancies and four Y atoms into the supercell, which corresponds to a 12.5% Y concentration, to study $V_{\ddot{O}}$-$V_{\ddot{O}}$ interaction. As an example, we choose the configuration of two lowest-energy 11[YY-1] Y-$V_{\ddot{O}}$-Y trimer units in the supercell to study the $V_{\ddot{O}}$-$V_{\ddot{O}}$ (i.e., trimer-trimer) interaction. Table 2.3 shows the relative energies for several possible oxygen vacancy separations.

Unlike Eichler's[17] finding that oxygen vacancies prefer to stay as far as possible without directional preference, our results show that oxygen vacancies in tetragonal YSZ also prefer to form pairs as they do in cubic YSZ, but with different direction of alignment, favoring the [1,$\frac{1}{2}$,0] alignment instead of the <1, $\frac{1}{2}$, $\frac{1}{2}$> alignment in cubic YSZ.

2.3.2.2.3 Defect configuration of two doping unit pairs: $V_{\ddot{O}}V_{\ddot{O}}$ pair- $V_{\ddot{O}}V_{\ddot{O}}$ pair interaction. Given the formation of the [1,$\frac{1}{2}$,0] aligned $V_{\ddot{O}}V_{\ddot{O}}$ pairs in tetragonal YSZ, we then studied the $V_{\ddot{O}}V_{\ddot{O}}$ pair- $V_{\ddot{O}}V_{\ddot{O}}$ pair interactions at even high Y concentration. Again, we introduced four oxygen vacancies and eight Y atoms into the supercell corresponding to a 25% Y concentration. Since we already knew from the studies of cubic YSZ that oxygen vacancy pairs repel each other, we first choose the [0,1,1] direction, because it gives the largest pair-pair separation distance. Then we tested pairs of different alignments, shown as case 1 in Table 2.3. Note that in tetragonal lattice, the [0, 1, 1] direction is longer than the [1,1,0] direction, while in cubic lattice all the <0,1,1> directions have the same distance. Although the single "isolated" $V_{\ddot{O}}V_{\ddot{O}}$ pair favors the [1,$\frac{1}{2}$,0] alignment at low Y concentration, interestingly, we found that the pair-pair interaction changes the preferred pair alignment into [1,$\frac{1}{2}$, $\frac{1}{2}$] direction at high Y concentration, as shown in Table 2.3. The main reason for such change of oxygen vacancy pair alignment is found to be associated with the change of lattice parameters with the increasing Y concentration. The tetragonal lattice tends to become more cubic like (i.e., decreasing *c*/*a* ratio and decreasing *dz*, see more discussion below) at high Y concentration, which converts the oxygen vacancy pair alignment to what has been found in the cubic case, i.e., the [1,$\frac{1}{2}$, $\frac{1}{2}$] alignment. Next, we fix the [1, $\frac{1}{2}$, $\frac{1}{2}$] pair alignment and

calculated the interaction energies between two such pairs along different directions, listed as case 2 in Table 2.3. Again, we found that the [0,1,1] pair-pair separation gives the lowest energy, as it gives the greatest $V_{\ddot{O}}$-$V_{\ddot{O}}$ separation, confirming the repulsive nature of pair-pair interaction.

In summary, comparing with the defect interactions in cubic YSZ, in tetragonal phase, Y atoms do not definitely have the largest separation in a Y-$V_{\ddot{O}}$-Y trimer doping unit, but choose the smallest $V_{\ddot{O}}$-Y separation of larger attraction to partially compensate the Y-Y repulsion at shorter distances, such as the 11[YY-1] configuration; oxygen vacancies form pairs along <1,$\frac{1}{2}$,0> at low concentration and transform to the <1, $\frac{1}{2}$, $\frac{1}{2}$> direction at high Y concentration, which is correlated with the change of lattice parameters with the increasing Y concentration.

2.3.3 Correlation of Microscopic Defect Configuration with Macroscopic Phase Transition and Lattice Properties in Cubic and Tetragonal YSZ

From a computational point of view, one reason for the existence of large controversies with respect to the defect-defect interactions and defect configurations in YSZ is because calculations are done with different methods and different computational and system setups, and there is no good way to validate a given calculation result, especially as the energy differences between different defect configurations are often very small in the same order of computational accuracy. Generally, the first-principles calculations suffer from limitations of system size and periodic boundary conditions. For ionic solids, the supercell size must be larger than the electrostatic screening length, typically in the order of a few nanometers for YSZ[41]. Periodic boundary conditions are restricted in treating real defect distributions which are random. Another difficulty is that

direct comparison between the computations and experiments is limited because the microscopic experimental data of atomic defect configurations of YSZ are limited and sometimes nonconclusive. To circumvent these difficulties, we adopt here a different strategy to validate our computation results. We use the optimized microscopic atomic defect configurations as inputs to calculate the macroscopic properties of relative phase stability and lattice parameters of cubic and tetragonal YSZ as a function of Y concentration, then compare the resulting macroscopic properties with the experiments. These macroscopic properties are much easier to measure experimentally so that more abundant and reliable experimental data are available for comparison.

2.3.3.1 Relative Phase Stability of Cubic and Tetragonal YSZ

In calculating the phase stability, we optimized all the cell parameters subject to the given lattice symmetry (i.e., cubic vs. tetragonal) and internal atomic coordinates subject to the given defect configurations (i.e., the lowest-energy ones). Fig. 2.2 shows the relative phase stability of cubic and tetragonal YSZ vs. Y concentration. The phase transition from tetragonal to cubic phase is predicted to occur at ~10% Y concentration with the increasing Y concentration. This is in good agreement with the experiment which reported that YSZ can be partially stabilized in the tetragonal phase at low Y concentration and fully stabilized in the cubic phase above 8% to 15% Y concentration [5].

At low Y concentration below the phase transition point (~10% Y concentration), the tetragonal phase is more stable because the pure ZrO_2 favors the tetragonal phase. Above the transition point, the cubic phase becomes more stable, and the largest energy difference between the cubic and tetragonal phase occurs at 18.75% Y concentration, as shown in Fig. 2.2. We observe empirically an interesting correlation between the relative

stability of cubic vs. tetragonal phase and the difference of oxygen displacement between cubic and tetragonal YSZ, as shown in Fig. 2.3. The oxygen displacement (*du*) in cubic YSZ is completely induced by doping and occurs equally along all three crystallographic directions. The oxygen displacement (*dz*) in tetragonal YSZ is induced by both lattice distortion and doping and occurs dominantly along the z-axis. We found that in cubic YSZ, *du* first increases and then decreases with the increasing Y concentration, while in tetragonal YSZ, *dz* decreases monotonically with the increasing Y concentration, as shown in Fig. 2.3(a). In Fig. 2.3(b), the difference of oxygen displacement (Δdu) and the absolute value of the difference of relative energy ($|\Delta E|$) in cubic vs. tetragonal YSZ are plotted as a function of Y concentration, which shows that the energy difference between these two phases has a close correlation with the difference of oxygen displacement. As the Δdu shows a minimum difference in the range of 6.25-12.5% Y concentration, the $|\Delta E|$ displays also a minimum in about the same range of Y concentration where the phase transition occurs. Note that at high Y concentration of 25%, the energies of two phases become almost degenerate and the difference of oxygen displacements in the two phases is also very small. This is because at such high Y concentration, the tetragonal phase has a *c*/*a* ratio very close to 1.0 (see Fig. 2.4), becoming indistinguishable from the cubic phase. Experimentally, it has been observed that between 26% and 57% Y concentration[4], YSZ separates into a mixture of cubic YSZ and rhombohedra $Y_4Zr_3O_{12}$[42] and beyond 57% Y concentration, the $Y_4Zr_3O_{12}$ phase dominates[4]. Our calculations suggest that the observed phase separation starting at ~ 25% Y is possibly related to the fact that degenerate energy between the "tetragonal" and cubic phase at the 25% Y concentration and the cubic is not the solely stable phase at the high Y concentration.

2.3.3.2 Lattice Properties of Cubic and Tetragonal YSZ

Next we analyze the changes of lattice parameters as a function of Y concentration for both cubic (single parameter, *a*) and tetragonal (two parameters, *a* and *c*) phases and compare our calculations with experiments. Figure 2.4(a) shows that the lattice constant of the cubic phase increases almost linearly with the increasing Y concentration, with a linear fit of $a = 5.049 + 0.233\ x$ in the range of $0.0625 < x < 0.25$ (see solid line in Fig. 2.4(a), x is the Y concentration), which is in good agreement with the experimental result of $a = 5.104 + 0.204\ x$ $(0.18 < x < 0.90)$[43]. This linear dependence indicates a uniform lattice expansion upon Y doping, which in turn suggests that doping is isotropic without any directional preference and defect distribution is completely random. This is because although there are specifically favored alignments of oxygen vacancy pairs and directions of pair-pair interactions, as we discussed in section 2.2A, there are an equal number of equivalent alignments and directions along all three crystallographic axes in the cubic phase. Consequently, the overall average doping effect has no directional preference, leading to isotropic doping and uniform lattice expansion.

The situation is different for the tetragonal phase because of the lower lattice symmetry. Figure 2.4(a) shows that for the tetragonal YSZ, the lattice constant *a* increases with the increasing Y, with a linear fitting of $a = 5.051+0.248\ x$ in the range of $0.0625 < x < 0.1875$ (solid line in Fig. 2.4(a)), which agrees well with the experimental result in the same range of x, $a = 5.080 + 0.349\ x$ $(0.05 < x < 0.13)$[43]. The lattice constant *c* first decreases, and then increases with the increasing Y concentration, and for the decreasing regime the linear fitting gives $c = 5.107 – 0.229\ x$ $(0.0625 < x < 0.125)$, which is in good agreement with the experimental result in the same range of, $c = 5.195 – 0.309$

x ($0.05 < x < 0.13$)[43]. For the increasing regime, the linear fitting gives $c = 5.074 + 0.034\,x$ ($0.125 < x < 0.25$). From the calculated lattice parameters a and c, we plotted the c/a ratio as a function of Y concentration in Fig. 2.4(b), which shows that the c/a ratio decreases monotonically with the increasing Y concentration. By ~ 10% Y concentration where phase transition from tetragonal to cubic phases occur, the c/a ratio of the tetragonal phase actually becomes very close to 1.0.

Next we try to understand why the lattice parameter c of the tetragonal phase first decreases and then increases with the increasing Y concentration. This intriguing behavior is found to be correlated with the the microscopic atomic defect configurations which evolve in two different regimes of oxygen vacancy arrangements and interactions at different Y concentrations. At low Y concentration (below 12.5%), the oxygen vacancies align predominantly in the $[1, \frac{1}{2}, 0]$ direction, rather than the $[0, 1, \frac{1}{2},]$ or $[1,0, \frac{1}{2}]$ direction (note that these three directions would be equivalent in the cubic lattice). This implies that oxygen vacancies occupy the x-y plane of oxygen atoms in the lattice, as shown in Fig. 2.5(a), rather than the x-z or y-z plane of oxygen atoms. Because the concentration of oxygen vacancies is relatively low, they only appear in one of every few x-y planes of oxygen. Notice that effectively, the x-y plane of oxygen with vacancies will become positively charged, which causes a relatively “attractive” interaction between the vacancy-occupied oxygen plane and its neighboring oxygen planes without vacancy, i.e., their interaction becomes less repulsive than that between two oxygen planes without vacancy. Consequently, this effective attraction causes a shrinkage of lattice along the z-direction and a decrease of lattice parameter c with the increasing Y concentration, as shown in Fig. 2.4(a). One may argue that Y is expected to also have an effect on lattice

due to its size and charge difference in replacing Zr. However, we found the Y atom does not have a strong site (alignment) preference as the $V_{\ddot{O}}$ does, as they occupy different 2NN positions to $V_{\ddot{O}}$. Consequently, the size and charge effect of Y is close to being homogenous, expanding the lattice more or less uniformly in all directions, so that it increases the lattice constant but without changing substantially the c/a ratio. For this reason, we attribute the change of c/a ratio mostly to the oxygen vacancy alignment.

In contrast, at high Y concentration (above 12.5%), the oxygen vacancies change to the $[1, \frac{1}{2}, \frac{1}{2}]$ alignment. This implies that oxygen vacancies must occupy two neighboring x-y planes simultaneously, as shown in Fig. 2.5(b). So effectively, these two x-y planes of oxygen with vacancies become positively charged, causing a relatively "repulsive" interaction between them in comparison to the situation of low Y concentration when only one isolated x-y plane of oxygen vacancy is effectively positively charged. Consequently, this effective repulsion causes an expansion of lattice along the z-direction and an increase of lattice parameter *c* with the increasing Y concentration, as shown in Fig. 2.4(a).

The above analysis illustrates that the macroscopic lattice properties are closely correlated with the microscopic atomic defect configurations in YSZ. Furthermore, the defect configurations and interactions we found might shed some light on explaining the experimentally observed ionic conductivity behavior. At low Y concentration (below 12.50%), oxygen vacancies are more mobile because individual $V_{\ddot{O}}$ and $V_{\ddot{O}}V_{\ddot{O}}$ pair within one single x-y plane of oxygen, as shown in Fig. 2.5(a), may jump within the same x-y plane or to the neighboring x-y planes of oxygen independently. At high Y concentration (above 25%), oxygen vacancies are less mobile because oxygen vacancies

simultaneously occupying two neighboring x-y planes of oxygen, as shown in Fig. 2.5(b), have to jump concertedly in a correlated manner to retain their low-energy [1, $\frac{1}{2}$, $\frac{1}{2}$] alignments. On the other hand, there are more oxygen vacancies available at high Y concentration than at low Y concentration. We speculate that the combination of two counteracting effects, oxygen vacancy mobility and concentration, are partially responsible for the ionic conductivity being maximum at Y concentration of 15%-18%[5].

2.4 Conclusions

We have performed a detailed first-principles study of atomic defect configurations in cubic and tetragonal YSZ as a function of Y concentration. In general, the defect configurations are found to be governed by the competition between the electrostatic interaction energies and strain energies, with the former being the most dominant effect. These are induced by different charge states and atomic sizes of the doped defects (ions and vacancies) from the host ions. At high Y concentrations, pairing and clustering of defects occur along preferred crystallographic directions that may vary with the increasing Y concentration to balance the change of electrostatic and strain energies. These changes in microscopic atomic defect configurations are shown to be closely correlated with the macroscopic properties of relative phase stability between the cubic and tetragonal phase of YSZ and their respective lattice properties. Such correlation also facilitates a direct comparison between our calculations and experiments, and provides an effective means to validate the computational results. Specifically, based on our optimized defect configurations, we correctly identified the tetragonal to cubic YSZ phase transition point and predicted the changes of lattice parameters with the increasing Y concentration, in good agreement with experiment.

2.5 Acknowledgements

We thank Christian Carbogno and Matthias Scheffler for their helpful discussions. We are grateful for the financial support from DOE EFRC Grant Number DE-SC0001061 as a flow through from the University of South Carolina.

2.6 References

[1] G. Teufer, *Acta Crystallogr.* **15**, 1187 (1962).

[2] O. Ruff and F. Ebert, Z. Anorg. *Allg. Chem.* **180**, 19 (1929).

[3] M. Yashima, K. Ohtake, M. Kakihana, H. Arashi, and M. Yoshimura, *J. Phys. Chem. Solids* **57**, 17 (1996).

[4] C. Pascual and P. Duran, *J. Am. Ceram. Soc.* **66**, 23 (1983).

[5] M. Yashima, K. Morimoto, N. Ishizawa, and M. Yoshimura, *J. Am. Ceram. Soc.* **76**, 1745 (1993).

[6] R. Krishnamurthy, Y.-G Yoon, D. J. Srolovitz, and R. Car, *J. Am. Ceram. Soc.*, **87**, 821 (2004).

[7] R. Devanathan, W.J. Weber, S.C. Singhal, and J.D. Gale, *Solid State Ionics* **177**, 1251 (2006).

[8] J.P. Goff, W. Hayes, S. Hull, M.T. Hutchings, and K.N. Clausen, *Phys. Rev. B* **59**, 14202 (1998).

[9] G. Stapper, M. Bernasconi, N. Nicoloso, and M. Parrinello, *Phys. Rev. B* **59**, 797 (1999).

[10] C.R.A. Catlow, A.V. Chadwick, G.N. Greaves, and L.M. Moroney, *J. Am. Ceram. Soc.* **69**, 272 (1986).

[11] D. Kmoyoji, A. Yoshiasa, T. Moriga, S. Emura, F. Kanamaru, and K. Koto, *Solid State Ionics* **50**, 291 (1992).

[12] P. Li, I-W. Chen and J. E. Penner-Hahn, *J. Am. Ceram. Soc.* **77**, 118 (1994).

[13] B.W. Veal, A.G. McKale, A.P. Paulikas, S.J. Rothman, and L.J. Nowicki, *Physica B+C* **150**, 234 (1988).

[14] S. Ostanin, A.J. Craven, D.W. McComb, D. Vlachos, A. Alavi, A.T. Paxton, and M.W. Finnis, *Phys. Rev. B* **65**, 224109 (2002).

[15] X. Xia, R. Oldman, and R. Catlow, *Chem. Mater.* **21**, 3576 (2009).

[16] M.S. Khan, M.S. Islam, and D.R. Bates, *J. Mater. Chem.* **8**, 2299 (1998).

[17] A. Eichler, *Phys. Rev. B* **64**, 174103 (2001).

[18] M. Weller, *Z. Metallkd.* **84**, 381 (1993).

[19] M.H. Tuilier**,** J. Dexpert-Ghys**,** H. Dexpert, and P. Lagarde**,** *J. Solid State Chem.* **69**, 153 (1987).

[20] D Steele and B E F Fender, *J. Phys. C: Solid State Phys.* **7**, 1 (1974).

[21] W.L. Roth**,** R. Wong**,** A.I. Goldman**,** E. Canova**,** Y.H. Kao, and B. Dunn**,** *Solid State Ionics* **18-19**, 1115 (1986).

[22] H. Morikawa,Y. Shimizugawa, F. Marumo, T. Harasawa, H. Ikawa, K. Tohji, and Y. Udagawa, *J. Ceram. Soc. Jpn.* **96**, 253 (1988).

[23] A. Bogicevia and C. Wolverton, *Phys. Rev. B* **67**, 024106 (2003).

[24] K. Kawata, H. Maekawa, T. Nemoto, and T. Yamamura, *Solid State Ionics* **177**, 1687 (2006).

[25] Z. R. Dai, Z. L. Wang, Y. R. Chen, H. Z. Wu, and W. X. Liu, *Philos. Mag. A* **73**, 415 (1996).

[26] R. Osborn, N.H. Andersen, K. Clausen, M.A. Hackett, W. Hayes, M.T. Hutchings, and J.E. MacDonald, *Mater. Sci. Forum* **7**, 55 (1986).

[27] S. Hull, T.D. Farley, A. Hackett, W. Hayes, R. Osborn, N.H. Andersen, K. Clausen, M.T. Hutchings, and W.G. Stirling, *Solid State Ionics* **28-30**, 488 (1988).

[28] A. Bogicevic, C. Wolverton, G. M. Crosbie, and E. B. Stechel, *Phys. Rev. B* **64**, 014106 (2001).

[29] A. Predith, G. Ceder, C. Wolverton, K. Persson, and T. Mueller, *Phys. Rev. B* **77**, 144104 (2008).

[30] P. Dalach, D.E. Ellis, and A. van de Walle, *Phys. Rev. B* **82**, 144117 (2010).

[31] V. Blum, R. Gehrke, F. Hanke, P. Havu, V. Havu, X. Ren, K. Reuter, and M. Scheffler, *Comp. Phys. Comm.* **180**, 2175 (2009).

[32] V. Havu, V. Blum, P. Havu, and M. Scheffler, *J. Comp. Phys.* **228**, 8367 (2009).

[33] J. P. Perdew and Y. Wang, *Phys. Rev. B* **45**, 13244 (1992).

[34] J. P. Perdew, K. Burke, and M. Ernzerhof, *Phys. Rev. Lett.* **77**, 3865 (1996).

[35] X. Zhao and D. Vanderbilt, *Phys. Rev. B* **65**, 075105 (2002).

[36] B. Kralik, E.K. Chang, and S.G. Louie, *Phys. Rev. B* **57**, 7027 (1998).

[37] C.J. Howard, R.J. Hill, and B.E. Reichert, *Acta Crystallogr.* B**44**, 116 (1988).

[38] P. Aldebert and J. P. Traverse, *J. Am. Ceram. Soc.* **68**, 34 (1985).

[39] S. Fabris, A. Paxton, and M.W. Finnis, *Acta Mater.* **50**, 5171 (2002).

[40] R.D. Shannon, *Acta. Cryst.* **A32**, 751 (1976).

[41] J. Maier, Prog. *Solid State Chem.* **23**, 171 (1995).

[42] S.P. Ray, V.S. Stubican, and D. E. Cox, *Mat. Res. Bull.* **15**, 1419 (1980).

[43] R. P. Ingel and D. Lewis 2.3, *J. Am. Ceram. Soc.* **69**, 325 (1986).

Table 2.1 Calculated and experimental ZrO_2 lattice and structural parameters. Energy of monoclinic phase is set as the reference of zero energy.

Lattice properties	This Work	PP LDA[35]	PP LDA[9]	PP LDA[36]	Experiment[37,38]
Cubic					
a (Å)	5.031	5.037	5.078	5.035	5.090
V ($Å^3/ZrO_2$)	31.84	32.10	32.73	31.91	32.97
B_0 (GPa)	272		268		194-220
E (eV/ZrO_2)	0.094		0.111	0.102	0.120
Tetragonal					
a (Å)	5.037	5.030	5.087	5.039	5.050
c (Å)	5.112	5.100	5.162	5.104	5.182
c/*a*	1.015	1.014	1.015	1.013	1.026
dz	0.043	0.042	0.042	0.042	0.0574
V ($Å^3/ZrO_2$)	32.43	32.26	33.39	32.41	33.04
B_0 (GPa)	234		197		190
E (eV/ZrO_2)	0.044		0.063	0.057	0.057
Monoclinic					
a (Å)	5.093	5.108		5.086	5.151
b (Å)	5.176	5.170		5.208	5.212
c (Å)	5.244	5.272		5.226	5.317
β (deg)	99.10	99.21		99.21	99.23
x(Zr)	0.2771	0.2769	0.2769	0.2779	0.2754
y(Zr)	0.0421	0.0422	0.0430	0.0418	0.0395

Table 2.1 Continued

z(Zr)	0.2101	0.2097	0.2100	0.2099	0.2083
x(O_1)	0.0710	0.0689	0.0640	0.0766	0.0700
y(O_1)	0.3370	0.3333	0.3237	0.3488	0.3317
z(O_1)	0.3420	0.3445	0.3524	0.3311	0.3447
x(O_2)	0.4493	0.4495	0.4497	0.4471	0.4496
y(O_2)	0.7575	0.7573	0.7560	0.7588	0.7569
z(O_2)	0.4807	0.4798	0.4790	0.4830	0.4792
V ($Å^3/ZrO_2$)	34.13	34.35	35.04	34.16	35.22
B_0 (GPa)	267		185		95-189

Table 2.2 Defect interactions in cubic YSZ.

$V_{\ddot{O}}$-Y	NN/NN	2NN/2NN	3NN/3NN	NN/2NN	NN/3NN	2NN/3NN
E (eV)	0.32	0	0.51	0.24	0.08	0.16

Y-Y	YY-1	YY-2	YY-3
E (eV)	0.17	0.03	0.00

$V_{\ddot{O}}$-$V_{\ddot{O}}$	$\langle\frac{1}{2},0,0\rangle$	$\langle\frac{1}{2},\frac{1}{2},0\rangle$	$\langle\frac{1}{2},\frac{1}{2},\frac{1}{2}\rangle$	<1,0,0>	$\langle1,\frac{1}{2},0\rangle$	$\langle1,\frac{1}{2},\frac{1}{2}\rangle$	<1,1,0>	$\langle1,1,\frac{1}{2}\rangle$	<1,1,1>
E (eV)	0.41	0.64	0.95	1.17	0.02	0.00	0.71	0.78	0.85

$V_{\ddot{O}}V_{\ddot{O}}$ pair-$V_{\ddot{O}}V_{\ddot{O}}$ pair case 1	$\langle0,\frac{1}{2},\frac{1}{2}\rangle$	<1,0,0>	$\langle0,\frac{1}{2},1\rangle$	$\langle\frac{1}{2},1,\frac{1}{2}\rangle$	<0,1,1>
E (eV)	1.02	0.94	0.72	0.58	0.00

$V_{\ddot{O}}V_{\ddot{O}}$ pair-$V_{\ddot{O}}V_{\ddot{O}}$ pair case 2	<1,0,0>	$\langle1,\frac{1}{2},0\rangle$	$\langle1,\frac{1}{2},\frac{1}{2}\rangle$	<1,1,0>
E (eV)	2.31	0.87	0.00	1.51

Table 2.3 Defect interactions in tetragonal YSZ.

Y-Y	11[YY-1]	22 [YY-3]	22 [YY-1]	33 [YY-3]	33 [YY-1]	44[YY-1]	13[YY-3]	12[YY-2]
E (eV)	0.04	0.05	0.15	0.12	0.20	0.29	0.00	0.09
$\boldsymbol{V_{\ddot{O}}}$**-**$\boldsymbol{V_{\ddot{O}}}$	[1,0,0]	[0,1,0]	[0,0,1]	$[1,0,\frac{1}{2}]$	$[0,1,\frac{1}{2}]$	$[1,\frac{1}{2},0]$	$[1,\frac{1}{2},\frac{1}{2}]$	$[\frac{1}{2},\frac{1}{2},1]$	[1,1,1]
E (eV)	1.44	1.44	1.53	0.19	0.19	0.00	0.14	0.75	0.77
$\boldsymbol{V_{\ddot{O}}V_{\ddot{O}}}$ **pair-**$\boldsymbol{V_{\ddot{O}}V_{\ddot{O}}}$ **pair case 1**			$[1,\frac{1}{2},0]$			$[1,\frac{1}{2},\frac{1}{2}]$		
E (eV)			0.43			0.00		
$\boldsymbol{V_{\ddot{O}}V_{\ddot{O}}}$ **pair-**$\boldsymbol{V_{\ddot{O}}V_{\ddot{O}}}$ **pair case 2**		$[\frac{1}{2},\frac{1}{2},1]$		$[\frac{1}{2},1,\frac{1}{2}]$			[0,1,1]	
E (eV)		0.63		0.21			0.00	

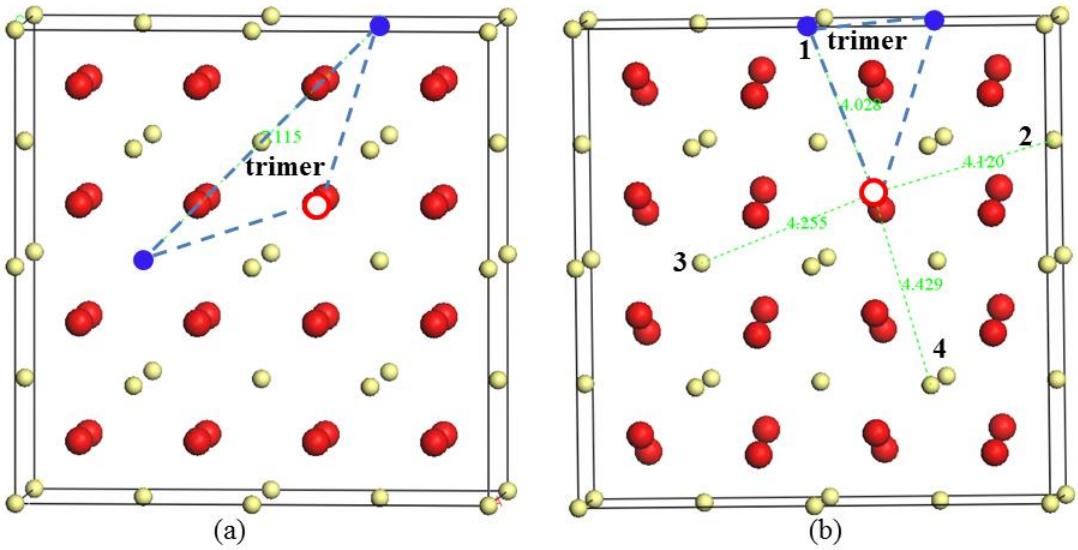

Fig. 2.1 The most stable defect configuration of a Y-$V_{\ddot{O}}$-Y trimer basic unit in (a) cubic and (b) tetragonal YSZ. Zr atoms are small (yellow) balls, oxygen atoms are large (red) balls, Y atoms are medium (blue) balls, and oxygen vacancy is a (red) open circle. The numbers in (b) mark the different distances of 2NN cation sites to the oxygen vacancy.

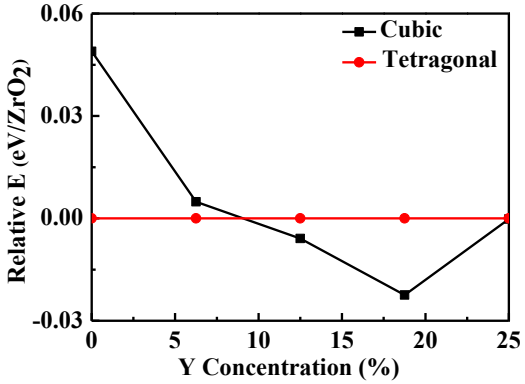

Fig. 2.2 Relative energy of cubic and tetragonal YSZ vs. Y concentration. The tetragonal phase is set as the reference of zero energy.

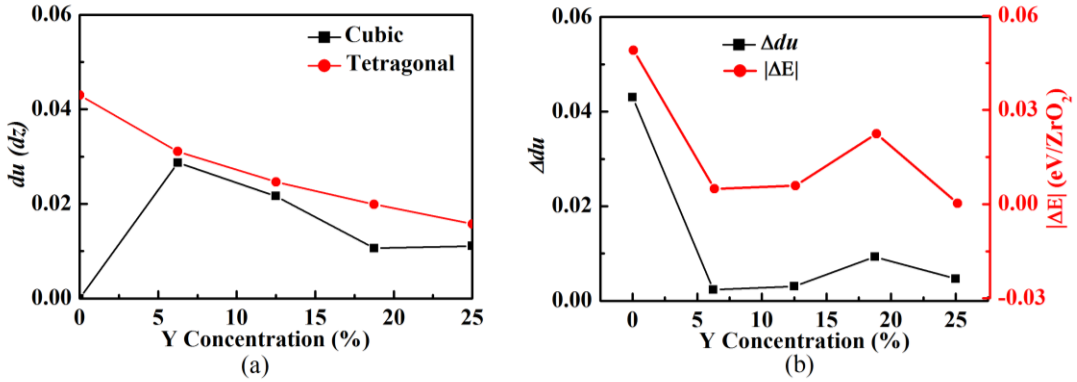

Fig. 2.3 The change of internal parameters. (a) The internal parameter *du* in cubic and *dz* in tetragonal YSZ; (b) The difference in internal parameter Δ*du* vs. Y concentration (Δ*du* = *dz*(tetragonal) - *du*(cubic) and |ΔE| = |E(tetragonal) – E(cubic)|).

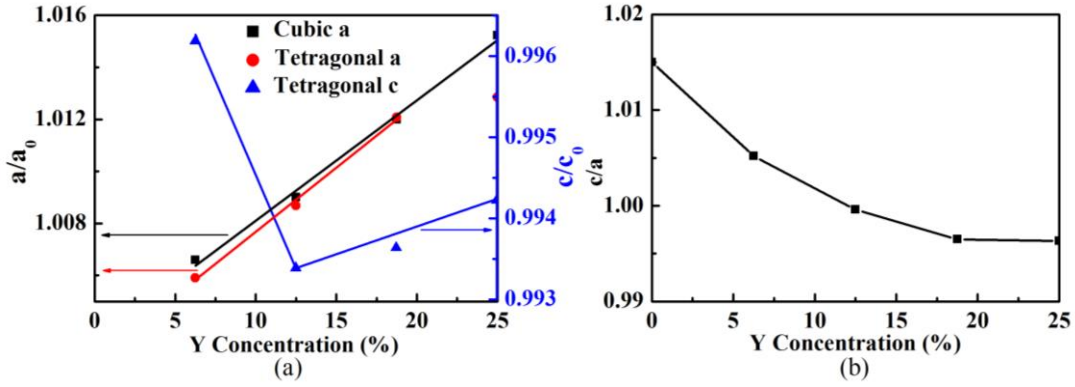

Fig. 2.4 The change of lattice parameters. (a) The lattice constants of cubic and tetragonal YSZ vs. Y concentration (in units of pure ZrO_2 lattice constants, a_0 and c_0). The solid lines are the linear fits for given Y concentration regimes; (b) The c/a vs. Y concentration in tetragonal YSZ.

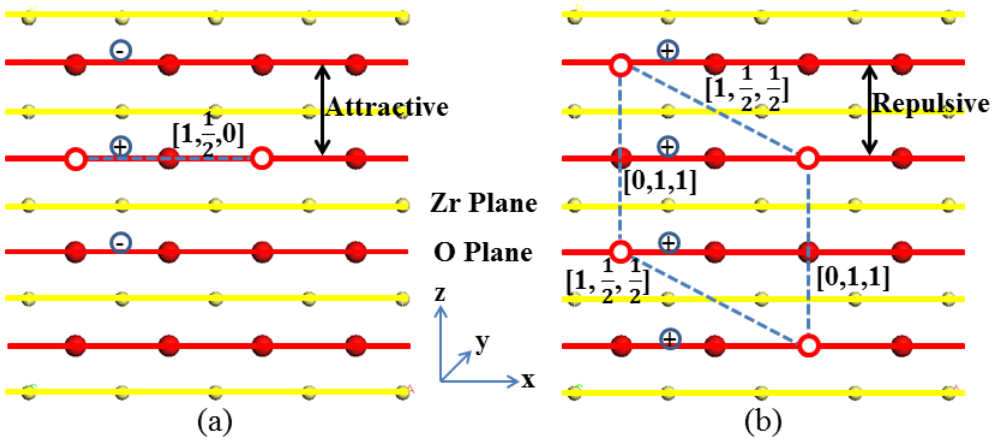

Fig. 2.5 Schematic demonstration of the alignments of oxygen vacancies. (a) Low Y concentration oxygen vacancy alignment in tetragonal YSZ; (b) high Y concentration oxygen vacancy alignment in tetragonal YSZ. Zr/Y atoms are small (yellow) balls, oxygen atoms are large (red) balls, and oxygen vacancies are (red) open circles.

CHAPTER 3

SUPPRESSION OF SR SURFACE SEGREGATION IN $LA_{1-X}SR_XCO_{1-Y}FE_YO_{3-\Delta}$: A FIRST PRINCIPLES STUDY

3.1 Introduction

Solid oxide fuel cells (SOFCs) have the potential to be a clean and efficient power generation technology; however, the high operating temperature often poses material durability and engineering challenges[1]. To lower the cost of SOFC technology (e.g., ~$150/KW by 2015[2]) and improve cell stability, it is necessary to reduce the operating temperature and use mixed electronic and ionic conductors as cathodes. In particular, $La_{1-x}Sr_xCo_{1-y}Fe_yO_{3-\delta}$ (LSCF) serves as a promising cathode material for intermediate-temperature SOFCs[3] because of its high electronic and ionic conductivity. However, the LSCF-based cathodes face severe efficiency degradation over time, typically at a rate of 0.05%/hour[4]. To date, a number of possible degradation mechanisms have been proposed, including interaction between LSCF and yttria-stabilized zirconia (YSZ) [5], Cr contamination[6], coarsening of the cathode microstructure[7], loss of conductivity[8], and the widely believed Sr surface segregation (SSS) in LSCF cathodes[9]. The enrichment of Sr at cathode surface may de-activate sites for oxygen reduction reaction and hence increase cathode resistance[10-12].

It has been widely reported that SSS occurs in many $La_{1-x}Sr_xBO_3$ (B is Co, Fe, Mn, etc.) perovskite cathode materials, leading to various product phases on the surface or interface. Heide et al.[13] reported a general Sr enrichment at all surfaces by a factor of ~1.2 to 2 times their stoichiometric values, forming SrO, then it may further react with CO_2 forming $SrCO_3$ at low temperatures. Elshof et al.[14] found that Sr segregates at both sides of the membrane, forming $SrCO_3$ and $SrSO_4$. Oh et al.[6] reported that the Sr segregation factor is approximately 2 and this is accompanied by the reduction in transition metal concentration at the surface, forming SrO and $SrCrO_4$. Mai et al.[5] found formation of insulating zirconate phases, such as $SrZrO_3$, in the LSCF cathode/YSZ electrolyte interface.

While SSS has been observed under various experimental conditions, the underlying mechanism is not completely clear, hindering the efforts to effectively suppress SSS. Several possible reasons have been proposed for SSS, such as kinetic demixing which is due to the greater mobility of Sr than other cations under oxygen partial pressure[11,12], acid-base reaction where electropositive Sr works as a base while O_2 and Cr vapor species serve as acids[6], different surface free energies and different atomic sizes[15], and surface charge effect due mainly to electrostatic contributions[16]. However, until now there has been no established generally accepted theory. More recently, Lynch et al.[17] reported that upon $La_{1-x}Sr_xMnO_3$ (LSM) coating on LSCF, there is no obvious observation of SSS. The suppression of SSS in LSCF under LSM coating opens a possibility to increase the cathode durability, making mechanism investigation crucial for guidance in future experiments. The Solid State Energy Conversion Alliance (SECA) requirement for SOFC efficiency degradation of less than 0.001%/hour[2], also calls for a

better understanding of the suppression of SSS.

For a typical surface, it is widely recognized that surface stress plays an important role in determining surface properties[18,19] and a flat, strain free surface is naturally unstable under sinusoidal surface perturbations having a wave number greater than a critical value[20], and strain relaxation can be partially accomplished by redistribution of ions with different sizes[21]. Also, it is well known that when there is an asymmetrically charged surface present in a crystal, the dipole moment perpendicular to the surface results in divergence of the long-range electrostatic interaction energy, making the surface unstable[22]. In principle, the polar surface can be stabilized by neutralizing the surface charge, such as via redistribution of ions with different charges. Hence, we expect that strain and surface charge will play an essential role in SSS in LSCF, because Sr and La have different charges and ionic radii.

To gain a better understanding of the underlying mechanisms for SSS and in the hope of finding ways to suppress SSS (important for developing high efficiency SOFCs), we have employed first principles density functional theory (DFT) computational method to systematically study SSS in LSCF. We first identified two basic thermodynamic driving forces for SSS, which are illustrated by studying the effect of strain and surface charge (through doping) on SSS. Then we suggest two common factors for suppressing SSS: applying compressive strain and reducing surface charge. We verified our findings by studying the dependence of SSS on oxygen vacancy formation, Co substitution of Fe and cation deficiency. Moreover, we provide a possible explanation for the recently observed LSM-coating effect on SSS in LSCF[17].

3.2 Computational Method

The spin-polarized calculations are performed using VASP[23], a plane wave based *ab initio* simulation package. The commonly used composition for LSCF is $La_{0.4}Sr_{0.6}Co_{0.2}Fe_{0.8}O_{3-\delta}$ in SOFCs due to its good thermomechanical stability. In order to reduce the system size, $La_{0.5}Sr_{0.5}Co_{0.25}Fe_{0.75}O_{3-\delta}$ was used in this study as a model system. Supercells of a 12-layer slab containing 2×1×6 of the ABO_3 primitive unit cell and 20 Å vacuum is constructed to model the LSCF surface. For the $La_{0.5}Sr_{0.5}MnO_3$ (LSM) coating, a 4-layer LSM is added (~1.5% lattice mismatch). To improve the accuracy of the calculation, a 4×8×1 k-point mesh and 800 eV kinetic energy cutoff (the hard potential for O is chosen) are used, which leads to an energy convergence within 1 meV/atom when a force convergence criterion of 0.01 eV/Å was used. Perdew-Burke-Ernzerhof (PBE) exchange-correlation functional with the projector-augmented-wave approach is used except for the B-site transition metal elements which are treated by the PBE+U method with U_{eff} = 3.3, 4.0, and 4.0 eV for Co, Mn, and Fe, respectively[24]. Dipole correction (~0.9 electron·Å) is added for all slab calculations. Charge analysis is done by the Bader charge analysis tool[25]. In studying the strain effect, in-plane lattice constants of the slab (normal to surface) are systematically changed for given bi-axial strain values while the z-coordinates of all atoms are fully relaxed. This may correspond to the situation where the SSS predominantly occurs in surface regions with the underneath bulk remaining intact, so that effectively surface layers are strained by the underlying bulk. To theoretically study the effect of strain due to oxygen vacancy, Co substitution of Fe, and doping of other elements, the in-plane lattice constants of the slab are fixed at the computational equilibrium LSF lattice constants with all the internal

atomic coordinates optimized.

As the first attempt, we focus our study on the SSS at the clean surfaces of a single phase of LSCF. In real SOFC operation, SSS actually occurs at the cathode/electrolyte (e.g., LSCF/YSZ) interfaces, so that the presence of YSZ may play an important role in affecting the SSS. However, we believe the fundamental knowledge we learn from the simpler case of SSS in LSCF may still shed some light on understanding the more complex process of SSS in the SOFC operation. We also note that another relevant phenomenon to the SSS is SrO phase separation. It is reported that LSCF reacts with YSZ forming $SrZrO_3$[5] while it does not react with gadolinia doped ceria (GDC)[26]. Consider the following two reactions:

$$SrO + ZrO_2 = SrZrO_3 \quad (3.1)$$

$$SrO + CeO_2 = SrCeO_3, \quad (3.2)$$

which describe the chemical reaction of LSCF in contact with YSZ and GDC, respectively. Assuming the activities of ZrO_2, CeO_2, $SrZrO_3$, and $SrCeO_3$ to be 1 and using Gibbs free energy data[27] derived at 1100 K, we obtain the activity of SrO to be 5.45×10^{-5} for reaction (1) and 4.61×10^{-3} for reaction (2), respectively. This suggests that the activity of SrO in LSCF is between 5.45×10^{-5} and 4.61×10^{-3}, indicating there is no obvious SrO phase separation for LSCF itself in the absence of YSZ or other oxide with which it reacts. We will leave the effect of YSZ on SSS and SrO phase separation for future studies. We also note that all of our calculations are performed at 0 K. Future studies will be directed to using *ab initio* thermodynamics approaches[28-30], to treat real SOFC operating conditions (temperature and partial oxygen pressure).

3.3 Results and Discussion

3.3.1 Thermodynamic Driving Force for SSS

We first examined the properties of bulk $La_{0.5}Sr_{0.5}FeO_{3-\delta}$ (LSF) as a benchmark. The LSF displays a tetragonal structure (a = 5.462 Å; c = 7.743 Å) with the A-site cations forming a layered structure consisting of alternating LaO and SrO planes. It is known that the A-site cations take a random distribution at high temperature[31], but our DFT calculations at zero temperature are done using the ordered layered structure which is found to be more stable than the homogenous distribution without entropic contribution and our unit cell size is too small to truly represent a random configuration. The ordered structure at low temperature is consistent with a previous study[32] suggesting that there is a significant size mismatch between A-site cations and the experimental observation of La-rich and Sr-rich cluster formation in Sr-doped $LaMnO_3$[33]. For the ideal LSF system, ferromagnetic and G-type antiferromagnetic are found to have similar energy (ferromagnetic phase is ~0.005 eV/cell lower). Huang et al. reported that $La_{0.58}Sr_{0.4}Co_{0.2}Fe_{0.8}O_{3-\delta}$ displays a ferromagnetic state below 200 K[34], but the magnetic state may still change with temperature, ion deficiency, concentration of Co, strain, distribution of A-site cations and at the surface. For simplicity, we opt to use the ferromagnetic state for all calculations. When only one oxygen vacancy ($V_{\ddot{O}}$, denoted using Kröger-Vink notation) is introduced, it prefers to occupy the LaO layer due to the largest $V_{\ddot{O}}$-B bond length which is opposite to the $V_{\ddot{O}}$ - Sr'_{La} (Sr substitution of La) coupling as generally supposed. Also, there is a preference for the $V_{\ddot{O}}$ to locate closer to Co than Fe, because Fe (+1.88) prefers to be in a higher charge state than Co (+1.43), and the bond length of Co-$V_{\ddot{O}}$ (1.918 Å) is smaller than Fe-$V_{\ddot{O}}$ (1.958 Å) so that Co more

easily accepts the extra charge left by $V_{\ddot{O}}$. This is in agreement with the experiment[35] and previous theoretical studies[36]. When more $V_{\ddot{O}}$ are introduced, the preference for the single $V_{\ddot{O}}$ to occupy the LaO layer is mitigated, pairs of $V_{\ddot{O}}$ are found to prefer to occupy the opposite corner of the oxygen octahedron of a B cation. The $V_{\ddot{O}}$ concentration in our calculation ranges from 1.43×10^{21} cm^{-3} to 2.86×10^{21} cm^{-3}.

Based on the above basic bulk properties and atomic configurations of LSCF, surface energy calculations of the low-index {001} (AO-BO_2), {110} (O_2-ABO), and {111} (B-AO_3) showed that the (001) orientation is most stable, which is chosen for the SSS calculations and analysis. In a (001) slab, one surface is terminated by the BO_2 plane, and the other surface by the AO plane, as shown in Fig. 3.1(a). The AO plane may consist of either LaO or SrO. To study SSS, for simplicity, we choose the LaO-terminated surface and then exchange the LaO atomic plane with one of the bulk SrO atomic plane in the middle of the slab as indicated in Fig. 3.1(a). More generally, partial exchange may occur which was not considered here. We then quantify the thermodynamic tendency of SSS by calculating the SSS energy as

$$E(seg) = [E(SrO) - E(LaO)]/2A \,, \tag{3.3}$$

where E(seg) is the SSS energy, E(LaO) is the system energy for the LaO-terminated surface, and E(SrO) is the system energy for the SrO-terminated surface with the SrO surface formed by exchanging the original LaO surface layer with one bulk SrO layer centered in the middle of slab. Clearly, a smaller E(seg) indicates a larger SSS. Note that there are two different surfaces in the slab but the BO_2 surface remains the same before and after SSS, so to a good approximation, we can assume the surface energy and surface

stress difference comes mainly from the AO surface only.

We identify two basic thermodynamic driving forces for SSS, surface stress/strain relaxation and surface charge minimization. First, the surface stress of the SrO-terminated surface is found to be smaller than that of the LaO-terminated surface (54 meV/Å^2 vs. 136 meV/Å^2 or 0.864 J/m^2 vs. 2.176 J/m^2), indicating better strain relaxation in the SrO-terminated surface. The better strain relaxation in the SrO-terminated surface can be associated with the fact that $La_{1-x}Sr_xFeO_3$ lattice constant decreases with increasing Sr concentration[35] so that the SrO surface layer relaxes strain more effectively under surface layer contraction condition. On the other hand, the surface charge of the SrO-terminated surface (+0.52*e*) is found notably smaller than that of the LaO-terminated surface (+1.35*e*). Thus, the combined effects of smaller surface stress and smaller surface charge make the SrO-terminated surface have lower surface energy than the LaO-terminated surface by 18 meV/Å^2 (0.288 J/m^2), driving Sr to segregate to the surface. We note that usually the absolute surface energy of solid surface falls in the range of ~100-500 meV/Å^2 (1.6-8 J/m^2). DFT calculations are able to predict the relative stability of different surface reconstructions with a small surface energy difference down to ~1 meV/Å^2 (0.016 J/m^2), such as the Si(001) surface reconstructions[37].

3.3.1.1 Effect of Strain on SSS in LSCF

To further reveal and understand the effect of strain on SSS, we have calculated the dependence of SSS energy on strain by applying biaxial strain in the surface plane, and results for LSF and LSCF slabs are shown in Fig. 3.1(b). Similar to surface diffusion stress[38,39] and adsorption stress[40] that underlies the effect of strain on surface diffusion and adsorption, we define a surface segregation stress as the surface stress difference

before and after the SSS:

$$\Delta\sigma = \sigma(SrO) - \sigma(LaO), \tag{3.4}$$

where σ(SrO) and σ(LaO) are the surface stress of the SrO- and LaO-terminated surface after and before the SSS, respectively. Following linear elasticity theory, the effect of strain on the SSS energy can be calculated as

$$E_{seg}^{\varepsilon} = E_{seg}^{\varepsilon=0} + (\Delta\sigma_{xx} + \Delta\sigma_{yy})\varepsilon, \tag{3.5}$$

where E_{seg}^{ε} is the SSS energy under strain (ε) and $E_{seg}^{\varepsilon=0}$ is the SSS without strain. So, to the first order, the SSS depends on strain linearly with a slope of surface segregation stress $\Delta\sigma$. The larger the $\Delta\sigma$ is, the stronger the strain dependence will be, and a given strain might either increase or decrease the SSS depending on the sign of $\Delta\sigma$. For LSF, our DFT+U calculations showed a small $\Delta\sigma$ ~ -42 meV/Å^2 (-0.672 J/m^2) indicating the SSS in LSF is weakly dependent on strain, which is indeed confirmed by our DFT+U calculations on applying strain, as shown in Fig. 3.1(b). For LSCF, $\Delta\sigma$ ~ -240 meV/Å^2 (-3.84 J/m^2) indicates a compressive surface segregation stress, namely the SSS tends to expand the surface, so that the SSS energy will decrease (increase) when a tensile (compressive) external strain is applied. This is again confirmed by DFT+U calculations as shown in Fig. 3.1(b). Therefore, a compressive strain will suppress the SSS in LSCF. This is consistent with the observation that the lattice constant of LSCF decreases nearly linearly with increasing Sr content[35] even though ionic radius of Sr is larger than that of La. Since strain always relaxes more effectively at a surface than in bulk, Sr prefers to stay in bulk under compressive strain and go to the surface under tensile strain.

Moreover, this should be generally applicable as long as the lattice constant decreases with the increasing Sr concentration in any $La_{1-x}Sr_xBO_3$ system; for example, Jalili et al.[41] reported the similar strain-dependent behavior of Sr segregation in $La_{1-x}Sr_xMnO_3$.

3.3.1.2 Effect of Surface Charge on SSS in LSCF

To reveal the effect of surface charge on SSS, we introduce dopants into the cation site in LSCF and calculate the corresponding change in the SSS energy. The dopant concentration in our calculation is 1.43×10^{21} cm^{-3}. The dopant can be introduced to replace either B-site or A-site cations. For the B-site doping, the dopants with a charge state higher than the replaced B-site cations (such as Zr and Y) favor the surface positions to minimize surface charge, while the dopants with a charge state lower than the replaced B-site cations (such as Li) favor the bulk positions again to minimize surface charge. For the A-site doping, the dopants are found to prefer the surface AO planes mainly because the dopants we considered have a much smaller ionic radius than the A-site cation ionic radius, so that the strain effect dominates giving their preferred surface position even though their charge states might favor the bulk position.

So, generally speaking, because of ionic size and charge state difference between the dopant and host atom, doping may affect the SSS due to both strain and charge effect. By introducing dopant with different charge states into the B-site, we found that the SSS is suppressed as a monotonic function of the absolute value of the BO_2 surface charge: the lower the absolute charge, the higher the SSS energy, as shown in Fig. 3.1(c). For the dopants with the same charge but different radii, it follows the expected strain dependence: the compressive strain suppresses the SSS, as shown in Fig. 3.1(c) for Al vs. Y and Ti vs. Zr. Doping of either the Co or Fe B-site show similar behavior, except the

subtle difference of slightly smaller positive charge of Co than Fe.

For doping of A-site with dopants of different charge state, the SSS energy is found to decrease monotonically with decreasing effective dopant charge state when the dopants are introduced into SrO layers, but increase monotonically with decreasing effective dopant charge state when the dopants are introduced into LaO layers, as shown in Fig. 3.1(d). This can be understood from the competition of occupying the surface AO layer by La vs. Sr. By reducing the LaO surface charge through doping of a lower valence element in the La-site, or conversely, increasing the SrO surface charge through doping of higher valence element in Sr-site, the difference between SrO and LaO surface charge is reduced, and hence the SSS is suppressed.

3.3.2 Ways for Suppressing SSS

Based on the basic driving forces we identified in the previous section, we suggest two possible ways to suppress SSS in LSCF: introduce compressive strain and reduce surface charge, which can be realized by following methods listed in Table 3.1. First, compressive strain can be applied either via introduction of larger dopant, or interface lattice mismatch between LSCF and certain electrolytes, or adding some surface coating layer that can provide compressive strain on LSCF. Second, dopant can be introduced into the cation site to alter the surface charge as needed, specifically, decreasing LaO or BO_2 surface charge, or increasing SrO surface charge. In addition, Co substitution of Fe, $V_{\ddot{O}}$ formation, and formation of A-site cation deficiency can be used to induce both strain and change of surface charge. While generally reducing the $V_{\ddot{O}}$ & Co content suppresses SSS, which is beneficial for SOFC cathode durability, on the other hand, it is worth noting that an optimized $V_{\ddot{O}}$ & Co content needs to be determined to reach a delicate

balance between keeping the appreciable suppression of SSS and maintaining the good mixed ionic and electronic conductivity of LSCF.

3.3.3 More on SSS and Suppression of SSS in LSCF

3.3.3.1 Effect of $V_{\ddot{O}}$ on SSS in LSCF

We first determine the preferred $V_{\ddot{O}}$ location by calculating the relative energy for $V_{\ddot{O}}$ occupying different AO layers, as denoted in Fig. 3.2(a). Fig. 3.2(b) and 3.2(c) show the calculated energies for LaO and SrO layer, respectively. In general, we found that $V_{\ddot{O}}$ favors the LaO layers over the SrO layers and the most stable location is the subsurface layer [denoted as "6-LaO" in Fig. 3.2(a)], which is set as the reference of zero energy. Also plotted are charge transfer and ionic relaxation, derived from the neighboring B-site cations of $V_{\ddot{O}}$, due to $V_{\ddot{O}}$ creation at different layers. It is a little surprising that ionic relaxation contribution to determining the $V_{\ddot{O}}$ position is negligible, which is opposite to what people normally think, like in YSZ[42]. A possible reason is that LSCF is a good electron conductor in which charge transfer is a more dominant effect than strain in affecting energy. We found that there is close correlation between the $V_{\ddot{O}}$ formation energy and charge transfer: the larger the charge transfer is, the lower the energy will be; the lowest energy configuration of $V_{\ddot{O}}$ in the subsurface 6-LaO layer shows the largest charge transfer. The reason that the largest charge transfer occurs in the subsurface layer is that the distance between $V_{\ddot{O}}$ and the neighboring surface B-cation is decreased relative to the bulk so that neighboring surface B-cations accept more charge while the cation octahedron surrounding $V_{\ddot{O}}$ remains intact, and this applies to all possible AO layer terminations. The same preferred $V_{\ddot{O}}$ location is found in LSCF, although the charge transfer upon $V_{\ddot{O}}$ creation appears relatively localized among the $V_{\ddot{O}}$-containing AO layer

and its neighboring layers in LSF, as shown by the charge difference plot in Fig. 3.3(a); the charge transfer spreads over the whole slab in LSCF, with all the Co atoms accepting extra charge from the electrons left by $V_{\ddot{O}}$ formation independent of the $V_{\ddot{O}}$-Co distance, as shown by the charge difference plot in Fig. 3.3(b).

Using the preferred $V_{\ddot{O}}$ location, we calculated the SSS in LSCF and found that $V_{\ddot{O}}$ slightly enhances the SSS lowering the SSS energy by ~1 meV/Å^2 (0.016 J/m^2). This qualitatively agrees with the experimental finding by Fister et al.[43] that the SSS becomes larger with decreasing oxygen pressure, since lower oxygen pressure should result in more $V_{\ddot{O}}$ in LSCF. To understand this enhancement, notice that $V_{\ddot{O}}$ introduction induces the following two changes. First, in terms of surface charge, the BO_2 surface becomes more negatively charged since it accepts the extra charge left by $V_{\ddot{O}}$ for being the neighboring layer of $V_{\ddot{O}}$, which drives the more positively charged LaO layer next to the BO_2 surface, leaving Sr behind to form the Sr-rich surface. The preferred $V_{\ddot{O}}$ occupation in the subsurface LaO layer makes the subsurface be mostly composed of La, leaving the surface AO layer to be more occupied by Sr as the A-site cations form alternating parallel planes. Second, in terms of strain, although the creation of $V_{\ddot{O}}$ causes compressive strain, consistent with previous findings[3], which would suppress SSS, the increased surface charge effect and the preferred subsurface location of $V_{\ddot{O}}$ make $V_{\ddot{O}}$ overall an enhancer for SSS.

3.3.3.2 Effect of Co on SSS in LSCF

When Co atoms are introduced to replace a quarter of Fe atoms in the slab, they prefer to stay in the bulk if no $V_{\ddot{O}}$ is present; but if $V_{\ddot{O}}$ is present in the surface, for the reason that $V_{\ddot{O}}$ prefers to form in the LaO subsurface layer and to be the nearest neighbor

of Co, more charge transfer can occur due to the shorter $V_{\ddot{O}}$-Co distance under surface contraction if Co atoms occupy surface sites. Similar to $V_{\ddot{O}}$, Co is found to enhance the SSS lowering the SSS energy by ~5 meV/Å^2 (0.08 J/m^2) for two reasons. First, in terms of strain, because the lattice constant of LSCF decreases with increasing Co content[44], Co doping induces tensile strain and tends to enhance SSS. Second, in terms of surface charge, the BO_2 surface becomes more negatively charged because the effective charge of Co is smaller than that of Fe, attracting La to the subsurface of the BO_2 terminated surface and leaving behind more Sr to occupy the AO-terminated surface at the same time, enhancing the SSS.

In addition, we found that although both $V_{\ddot{O}}$ and Co enhance the SSS separately, their combined effect lowering the SSS by ~3 meV/Å^2 (0.048 J/m^2) is smaller than the effect of Co alone. One possible reason for this is that $V_{\ddot{O}}$ and Co introduce opposite strain effects, the former compressive while the latter tensile; thus, compensating each other and thereby reducing the overall strain effect.

3.3.3.3 Introduction of Cation Deficiency

In experiment, cation deficiency is always used in trying to improve the performance of SOFCs, and Hansen et al.[45] reported that A-site deficient LSCF suppresses the SSS. Here, cation deficiency effect on SSS is studied for every cation species at the concentration of 1.43×10^{21} cm^{-3}, which is within experimental accessible values[45]. It is found that the A-site cation deficiency prefers to occur at the surface while the B-site cation deficiency occurs in bulk, mainly because of the surface charge minimization effect. As the stoichiometric AO surface is positively charged while the BO_2 surface is negatively charged, cation vacancy in the AO surface is favored as it decreases surface

charge while cation vacancy in the BO_2 surface is forbidden because it increases surface charge. Fig. 3.4(a) shows the energy difference, $\Delta E=E(bulk)-E(surface)$, where E(bulk) and E(surface) denote the system energy for cation deficiency with the cation removed from bulk and surface positions, respectively, along with the corresponding change of charge (Δq, red dots) and stress ($\Delta\sigma$, blue triangles). From the energy curve, we can see that the A-site deficiency favors surface positions (positive energy), while the B-site deficiency favors bulk positions (negative energy). We also see that the preferred cation deficiency position is mainly determined by surface charge minimization effect, as there is a close correlation between ΔE and Δq, but not so for $\Delta\sigma$, indicating the stress effect is less important here.

Fig. 3.4(b) shows the calculated SSS energy for different cation-deficiency configurations using the preferred A-site surface deficiency and B-site bulk deficiency positions as determined above (line connected data points, also both vacancy occupation in bulk (black squares) and on the surface (red circles) are provided for reference). We see that the A-site surface deficiency suppresses the SSS (positive segregation energy), while the B-site bulk deficiency enhances the SSS (negative energy). The A-site suppression can be understood in terms of a surface charge decrease, and the B-site enhancement in terms of introducing bulk tensile strain.

3.3.3.4 LSM-coating on LSCF

As recently reported by Lynch et al.[17], the LSM coating suppresses SSS in LSCF. It was found that Co goes to LSM, forming a hybrid $La_{1-x}Sr_xCo_{1-y}Mn_yO_{3-\delta}$ (LSCM) phase, and also $V_{\ddot{O}}$ concentration is increased in LSM. To better understand their experiments, we have performed first principles calculations to study the effect of LSM coating on the

SSS in LSCF and in particular to see whether the above-mentioned two factors can be applied in this case. Fig. 3.5(a) shows the preferred $V_{\ddot{O}}$ location between LSCF and LSM layers. Without Co, $V_{\ddot{O}}$ favors LSM (first data point); with Co only in LSCF but not LSM, $V_{\ddot{O}}$ favors LSCF (second data point); with Co in both LSCF and LSCM, $V_{\ddot{O}}$ favors LSCM (last three data points). This suggests that $V_{\ddot{O}}$ prefers to occupy sites next to Co, indicating a strong Co-$V_{\ddot{O}}$ binding, which is further shown by the increasing binding energy with the increasing Co concentration (last two data points). Fig. 3.5(b) shows the energy difference between Co in LSM/LSCM and in LSF/LSCF, using the latter as the reference of zero energy. Since $V_{\ddot{O}}$ prefers to be in LSM, as found in Fig. 3.5(a), we can conclude that Co prefers occupying LSM/LSCM, Fig. 3.5(b) (last two triangle data points). Fig. 3.5(c) shows the SSS energy in LSM coated LSCF for different $V_{\ddot{O}}$ and Co configurations. We see that $V_{\ddot{O}}$ and/or Co occupying LSM layers suppresses SSS. The more Co atoms locating at LSM, the stronger suppression of SSS in LSCF will be, regardless of the presence and location of $V_{\ddot{O}}$ (last three data points). Fig. 3.5(d) shows the overall LSM coating effect on the SSS energy in LSCF, calculated from the optimized $V_{\ddot{O}}$ and Co configurations. It clearly indicates that LSM-coating always strongly suppresses SSS in LSCF. The suppression is caused by the occupation of $V_{\ddot{O}}$ in LSM, the occupation of Co in LSM, and compressive strain under LSM coating (LSM 3.87 Å[46] vs. LSCF 3.93 Å[47]). Furthermore, because we exchanged the position of Co and Mn in the calculation for Co occupying LSM, the presence of Mn in LSCF introduces compressive strain which helps the suppression too. It is also interesting to point out that the magnitude of enhancement surprisingly decreases for the case with only $V_{\ddot{O}}$ introduced into the system even though $V_{\ddot{O}}$ occupying LSM tends to further suppress SSS

(first two data points). This is because an increased lattice constant of LSM and decreased lattice constant of LSF when $V_{\ddot{O}}$ is changed from LSF into LSM, leads to decreased compressive strain applied on LSF by LSM, thus hindering the suppression of SSS. These are consistent with experimental observations.[17]

On the other hand, it is also reported that by using PSM as coating layer[48], the performance enhancement is more significant. A possible reason is that, compared to LSM, the occupation preference of $V_{\ddot{O}}$ in the PrO layer is even stronger than that in the LaO layer. This is 0.20 eV lower according to our calculation, promoting more $V_{\ddot{O}}$ from LSCF into PSM coating layer, and hence inducing larger suppression of SSS in LSCF.

3.4 Conclusions

We have performed a systematic first principles study on SSS in LSCF. We found two basic thermodynamic driving forces for SSS: surface charge minimization and strain relaxation. Based on this finding, we suggest two possible ways to suppress SSS: applying compressive strain and reducing surface charge. We then illustrated several possibilities of affecting these two factors individually or together, through oxygen vacancy, Co substitution of Fe, and cation site deficiency. Finally, we applied our theoretical findings to explain recent experimental observations of suppression of SSS in LSCF by LSM and PSM coating in terms of these two factors. We believe that some of our findings on SSS and suppression of SSS are generally applicable in common perovskite $La_{1-x}Sr_xBO_3$ materials[49,50].

3.5 Acknowledgements

We thank Emily A. Carter for helpful discussions. We acknowledge the financial support from DOE EFRC Grant Number DE-SC0001061 as a flow through from the University of South Carolina. We also thank DOE-NERSC, Fusion at LCRC at Argonne National Laboratory, and CHPC at the University of Utah for providing computing resources.

3.6 References

[1] L. Yang, S. Z. Wang, K. Blinn, M. F. Liu, Z. Liu, Z. Cheng, and M. L. Liu, *Science* **326**, 126 (2009).

[2] S.D. Vora, Overview of DOE SECA Program, www.netl.doe.gov/publications/ proceedings/11/seca/pdf/Tue%20AM/Vora.2011_07_26_SECA.pdf

[3] S. Wang, M. Katsuki, M. Dokiya, and T. Hashimoto, *Solid State Ionics* **152-153**, 777 (2002).

[4] M. Becker, A. Mai, E. Iver-Tiffee, and F. Tietz, *Solid Oxide Fuel Cells*, p.514, *The Electrochemical Society Proceedings Series*, Pennington, NJ (2005).

[5] A. Mai, M. Becker, W. Assenmacher, F. Tietz, D. Hathiramani, E. Ivers-Tiffee, D. Stover, and W. Mader, *Solid State Ionics* **177**, 1965 (2006).

[6] D. Oh, E. Armstrong, D. Jung, C. Kan, and E. Wathsman, *ECS Transactions* **25**, 2871 (2009).

[7] P. Tanasini, M. CAnnarozzo, P. Costamagna, A. Faes, J. Van Herle, A. Hessler-Wyser, and C. Comninellis, *Fuel Cells* **9**, 740 (2009).

[8] C. Haering, A. Roosen, H. Schichl, *Solid State Ionics* **176**, 253 (2005).

[9] S. Li, W. Jin, P. Huang, N. Xu, J. Shi, and Y.S. Lin, *J. Membrane Sci.* **166**, 51 (2000).

[10] Z. Shao, and S.M. Haile, *Nature* **431**, 170 (2004).

[11] W. Jung, and H.L. Tuller, *Energy Environ. Sci.* **5**, 5370 (2012).

[12] E.J. Crumlin, E. Mutoro, Z. Liu, M.E. Grass, M.D. Biegalski, Y.L. Lee, D. Morgan, H.M. Christen, H. Bluhm, and Y. Shao-Horn, *Energy Environ. Sci.* **5**, 6081 (2012).

[13] P.A.W. V. Heide, *Surf. Interface Anal.* **33**, 414 (2002).

[14] J.E. Elshof, H.J.M. Bouwmeester, and H. Verweij, *Applied Catalysis A: General* **130**, 195 (1995).

[15] H. Dullli, P. A. Dowben, S. H. Liou, and E. W. Plummer, *Phys. Rev. B* **62**, R14629 (2000).

[16] W. A. Harrison, *Phys. Rev. B* **83**, 155437 (2011).

[17] M. E. Lynch, L. Yang, W. Qin, J. Choi, M. Liu, K. Blinn, and M. Liu, *Energy Environ. Sci.* **4**, 2249 (2011).

[18] F. Liu, in *Handbook of Theoretical and Computational Nanotechnology*, eds. M. Rieth and W. Schommers, **Chapter 10**, 577 (2006).

[19] F. Liu, M. Hohage, and M.G. Lagally, *Encyclopedia of Appl. Phys.*, eds. H. Immergut and G. Trigg, **Supplement Volume**, 321 (1999).

[20] M.J. Asaro, and W.A. Tiller, *Metall. Trans.* **3**, 1789 (1972).

[21] X.B. Niu, G.B. Stringfellow, and Feng Liu, *Phys. Rev. Lett.* **107**, 076101 (2011).

[22] W. Siemons, G. Koster, H. Yamamoto, W.A. Harrison, G. Lucovsky, T.H. Geballe, D.H.A. Blank, and M.R. Beasley, *Phys. Rev. Lett.* **98**, 196802 (2007).

[23] G. Kresse, J. Hafner, *Phys. Rev. B* **54**, 11169 (1996).

[24] L. Wang, T. Maxisch, and G. Ceder, *Phys. Rev. B* **73**, 195107 (2006).

[25] W. Tang, E. Sanville, and G. Henkelman, *J. Phys.: Condens. Matter* **21**, 084204 (2009).

[26] V. Dusastre, and J.A. Kilner, *Solid State Ionics* **126**, 163 (1999).

[27] I. Barin, *Thermochemical Data of Pure Substances*, VCH Publishers, **Third Edition** (2008).

[28] C. Lee, R. Behera, E. Wachsman, S. Phillpot, and S. Sinnott, *Phys. Rev. B* **83**, 115418 (2011).

[29] Y. Mastrikov, R. Merkle, E. Heifets, E. Kotomin, and J. Maier, *J. Phys. Chem. C* **114**, 3017 (2010).

[30] Y. Mastrikov, E. Heifets, E. Kotomin, and J. Maier, *Surf. Sci.* **603**, 326 (2009).

[31] Z.L. Wang, J. Zhang, *Phys. Rev. B* **54**, 1153 (1996).

[32] A. Chroneos, B. Yildiz, A. Tarancon D. Parfitt, and J.A. Kilner, *Energy Environ. Sci.* **4**,
2774 (2011).

[33] T. Shibata, B. Bunker, J.F. Mitchell, and P. Schiffer, *Phys. Rev. Lett.* **88**, 207205 (2002).

[34] B. Huang, J. Malzbender, and R.W. Steinbrech, *J. Mater. Rev.* **26**, 1388 (2011).

[35] L.-W. Tai, M.M. Nasrallah, H.U. Anderson, D.M. Sparlin, and S.R. Sehlin, *Solid State Ionics* **76**, 259 & 273 (1995).

[36] M. Pavone, A. M. Ritzmann, and E. Carter, *Energy Environ. Sci.* **4**, 4933 (2011).

[37] F. Liu, and M.G. Lagally, *Phys. Rev. Lett.* **76**, 3156 (1996).

[38] D.J. Shu, F. Liu, and X.G. Gong, *Phys. Rev. B* **64**, 245410 (2001).

[39] L. Huang, F. Liu, G.H. Lu and X. G. Gong, *Phys. Rev. Lett.* **96**, 016103 (2006).

[40] R. Pala, and F. Liu, *J. Chem. Phys.* **120**, 7720 (2004).

[41] H. Jalili, J.W. Han, Y. Kuru, Z. Cai, and B. Yildiz, *J. Phys. Chem. Lett.* **2**, 801 (2011).

[42] H. Ding, A.V. Virkar, and F. Liu, *Solid State Ionics* **215**, 16 (2012).

[43] T. Fister, D. Fong, J. Eastman, P. Baldo, M. Highland, P. Fuoss, K. Balasubramaniam, J. Meador, and P. Salvador, *App. Phys. Lett.* **93**, 151904 (2008).

[44] J.N. Kuhn, U.S. Ozkan, *Catalysis Letters* **121**, 179 (2008).

[45] K.K. Hansen, K.V. Hansen, *Solid State Ionics* **178**, 1379 (2007).

[46] S. Dussan, A. Kuman, and R.S. Katiyar, *MRS Proceedings*, 1199-F03-05 (2009).

[47] J.S. Hardy, J.W. Templeton, D.J. Edwards, Z. Lu, and J.W. Stevenson, *J. Power Sources* **198**, 76 (2012).

[48] D. Ding, M. Lynch, M. Liu, Y. Bai, W. Qin, M. Liu, $Pr_xSr_{1-x}MnO_{3-\delta}$ (PSM) and $La_{0.8}Sr_{0.2}Mn_{0.8}Co_{0.2}O_{3-\delta}$ (LSMC) Infiltrated LSCF Cathodes for SOFCs, netl.doe.gov/ publications/proceedings/11/seca/pdf/Poster%20Presentations/Ding.pdf

[49] S. Piskunov, E. Heifets, T. Jacob, E. Kotomin, D. Ellis, and E. Spohr, *Phys. Rev. B* **78**, 121406 (2008).

[50] E. Heifets, E. Kotomin, Y. Mastrikov, S. Piskunov, and J. Maier, in *Thermodynamics – Interaction studies - Solids, Liquids and Gases*, ed. J.C. Moreno-Pirajan, 491 (2011).

Table 3.1 Common factors for suppressing SSS.

(1) Apply compressive strain	Introduce larger dopant Apply epitaxial strain/coating	Reduce Co concentration Reduce $V_{\ddot{O}}$ concentration Create A-site deficiency
(2) Reduce surface charge	Decrease BO_2 surface charge Decrease LaO surface charge Increase SrO surface charge	

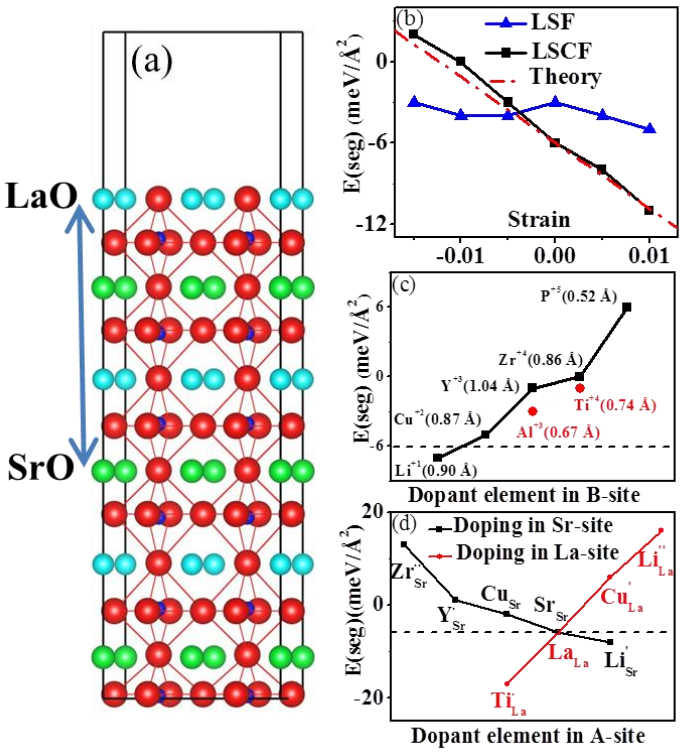

Fig. 3.1 Model of computational setups and results on SSS. (a) Illustration of SSS segregation with SrO exchanging with LaO indicated by the arrow. Cyan balls are La atoms, green are Sr, red are O, and small blue are Fe. (b) Effect of strain on SSS in LSF and LSCF. Squares are DFT+U calculated E(seg) and the dashed red line is the theory predicted dependence from Eq. 3.5 using the DFT+U calculated surface segregation stress. (c) Effect of the B-site dopant on SSS. (d) Effect of A-site dopant on SSS. The dotted horizontal line in (c) and (d) is E(seg) without doping.

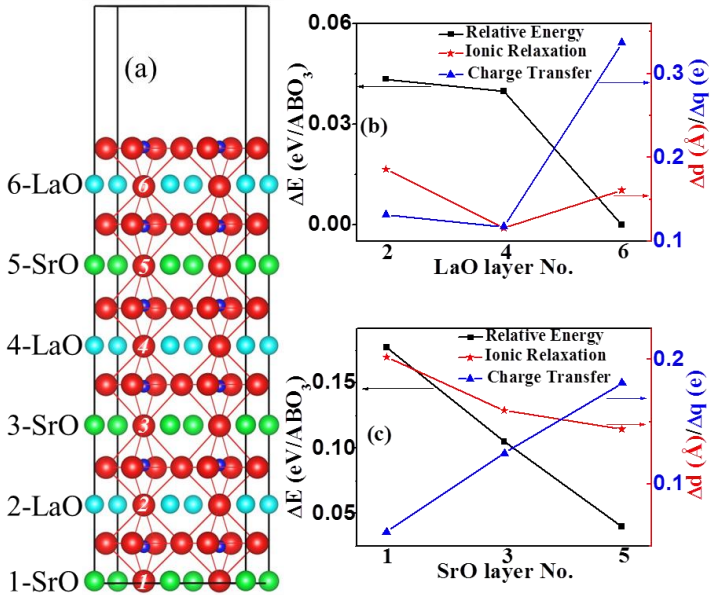

Fig. 3.2 AO layer definition and its properties. (a) The location of $V_{\ddot{O}}$ in LSF slab. Cyan balls are La atoms, green are Sr, red are O, and small blue are Fe. (b) LaO layer properties: squares are relative energy of $V_{\ddot{O}}$ located at different LaO layers as denoted in (a), with the "6-LaO" energy set as reference of zero energy, triangles are the corresponding charge transfer, and stars are ionic relaxation. (c) SrO layer properties, the symbols are the same as in (b).

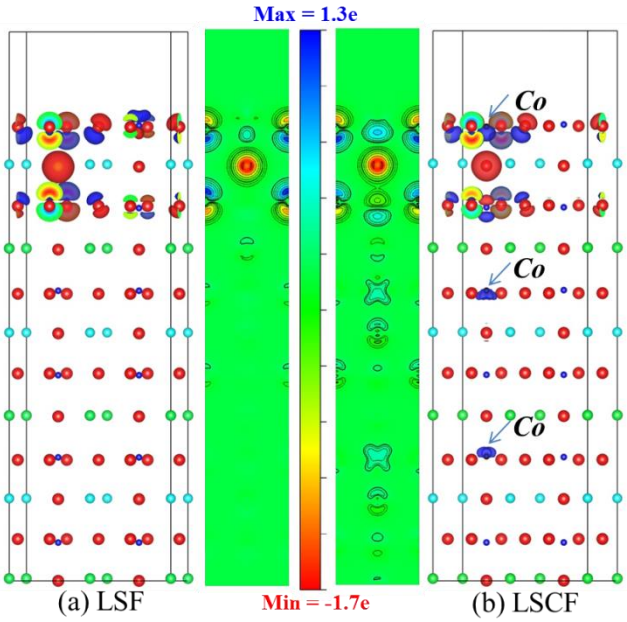

Fig. 3.3 Charge density difference plots upon $V_{\ddot{O}}$ formation. (a) LSF slab. (b) LSCF slab. Blue (red) cloud represents accepted (donated) charge. Cyan atoms are La, green atoms are Sr, red atoms are O, and small blue atoms are Fe; Co atoms are marked by arrows.

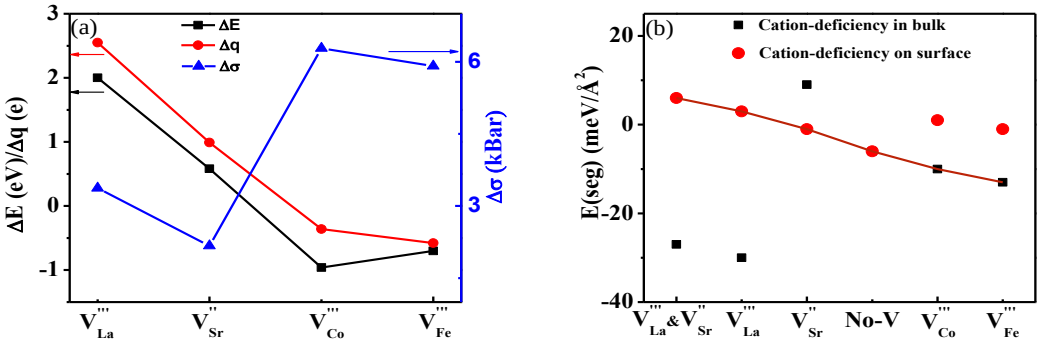

Fig. 3.4 Effect of introducing cation deficiency on SSS. (a) Cation-deficiency occupation position preference. Δq denotes difference of surface charge between vacancy occupying surface and bulk defined as q(bulk)-q(surface), Δσ denotes the decrease of system stress defined as σ(bulk)-σ (surface), and ΔE denotes change of system energy defined as E(bulk)-E(surface). (b) Effect of deficiency on SSS in LSCF; data on the line denote the preferred occupation sites.

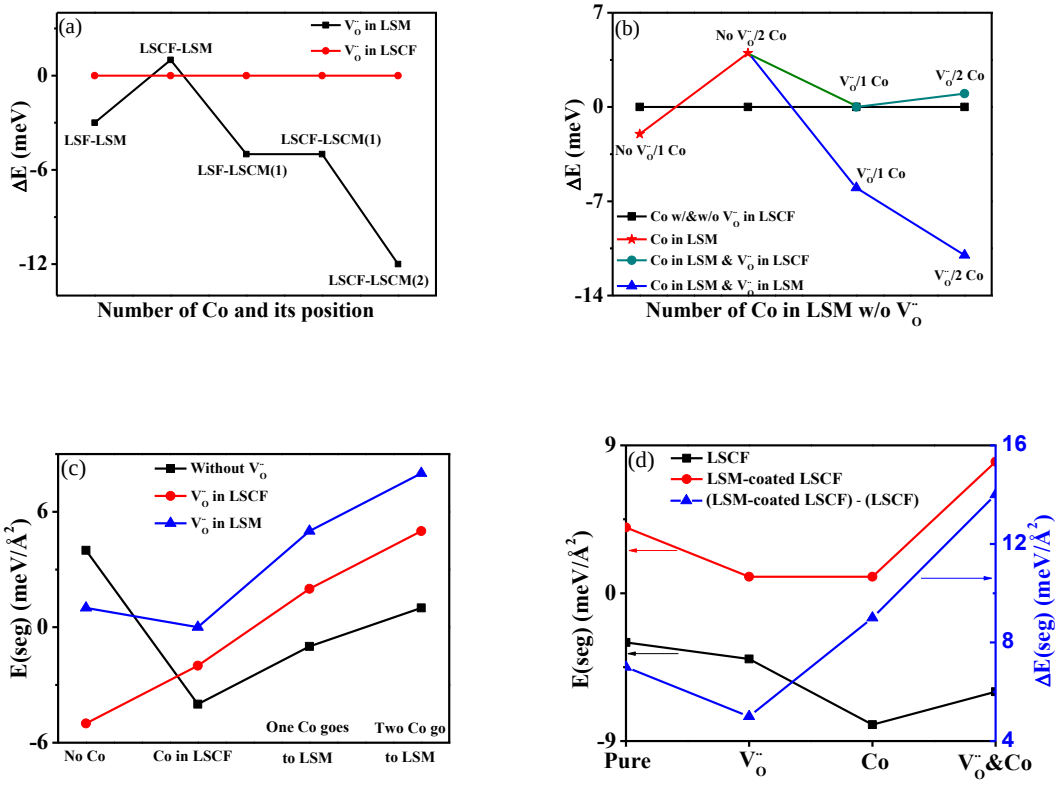

Fig. 3.5 SSS in LSM-coated LSCF. (a) The location of $V_{\ddot{O}}$ in LSM-coated LSCF, $V_{\ddot{O}}$ occupying LSCF is set as reference. *X* in "LSCM(*X*)" denotes the number of Co atoms in LSM. (b) The location of Co in LSM-coated LSCF, Co with/without $V_{\ddot{O}}$ occupying LSCF (and $V_{\ddot{O}}$ occupying LSCF if applicable) is set as reference. *X* in "*X* Co" denotes the number of Co atoms in LSM. (c) Effect of $V_{\ddot{O}}$ and Co location on SSS in LSM-coated LSCF. (d) Comparison of SSS between LSCF and LSM-coated LSCF, right y-axis and triangle data denote the E(seg) differences between LSCF and LSM-coated LSCF. $V_{\ddot{O}}$ (Co) denotes that only the oxygen vacancy (Co atom) was introduced into the system, and $V_{\ddot{O}}$&Co denotes that both are introduced into the system simultaneously.

CHAPTER 4

UNDERSTANDING CATION ORDERING AND OXYGEN VACANCY SITE PREFERENCE IN $BA_3CANB_2O_9$ FROM FIRST PRINCIPLES STUDIES

4.1 Introduction

Solid oxide fuel cells (SOFCs) directly convert the chemical energy into electrical energy with a high theoretical efficiency because it is not restricted by the Carnot cycle[1]. Coupled with the flexibility of fuel types and environmental friendly operations, SOFCs show great potential to fulfill the increasing energy demand for the future world[1]. The main hurdle limiting their commercialization is the high working temperatures, which increases the manufacture and material cost and accelerates the efficiency degradation, making the reduction of the operating temperature desirable[1,2]. However, a lower operating temperature leads to significant efficiency drop due to the high ohmic internal resistance in traditional oxygen ion conducting electrolyte, such as yttria-stabilized zirconia (YSZ).[3-5] Thus, a complex perovskite compound $Ba_3Ca_{1.18}Nb_{1.82}O_{9-\delta}$ (BCN18), which has attainable high proton concentration and high proton mobility,[6-8] to serve as a medium temperature proton conductor, has attracted broad interest[6-22].

Stoichiometric $Ba_3CaNb_2O_9$ (BCN) is a complex perovskite described by a general notation of $A_3B'B''_2O_9$, in which both A and B' are divalent, while B'' is

pentavalent (A and B or B'/B'' are used throughout this work with the same notations, if not specified). Oxygen vacancies ($V_{\ddot{O}}$) can be created either by alternating B'/B'' composition that deviates from the exact 1:2 ratio or by introducing acceptor dopants for charge compensation (e.g., Y^{3+} replacing Nb^{5+}). Proton conduction occurs when exposed to water vapor at high temperature due to the filling of the oxygen vacancy reaction[6-7]:

$$H_2O + V_{\ddot{O}} + O_O^x = 2OH_O, \tag{4.1}$$

where the equation is represented in the standard Kroger-Vink notation. The solubility of water at elevated temperature is reported as ~ 1/3 of the maximum theoretical value, so there might always be plenty of $V_{\ddot{O}}$ in the lattice during SOFC operations[7,16], though it is possible to remove most of the $V_{\ddot{O}}$ at high enough water vapor pressure. It is generally realized that the proton transport at least partly depends on its local atomic environment. This implies that B-site cation ordering and $V_{\ddot{O}}$ occupation site may play essential roles, making the study of the B-site cation ordering and $V_{\ddot{O}}$ position critical.

The atomic structure of BCN, especially the B-site cation ordering, has been widely studied in experiments. The crystal structure is reported to be in several polymorphs, including cubic[15,22,23], tetragonal[24], and trigonal (either in hexagonal or in rhombohedral)[15,18,21]. The latter two are slightly distorted from the cubic lattice. The B-site cations can be disordered, partially ordered, or fully ordered. The disordered distribution always results in a cubic unit cell[23,24], and the 1:1 ordering may result in a cubic or tetragonal unit cell[24], while the 1:2 ordering in <111> direction results in a trigonal unit cell[15,21]. The ordering may change with changing stoichiometric or the humidity of the environment, so does the unit cell structure[22,24]. Because various ordering

patterns exist, the understanding of the B-site cation ordering is still incomplete. Earlier studies[25,26] have shown the important role played by electrostatic effects between the different ionic species in driving the ordering process, while some recent works[21,27] suggested the ordering is due to the large ionic radius difference (~50%) between Ca^{2+} (1.14 Å) and Nb^{5+} (0.78 Å).

In the present work, we employ first principles calculations based on density functional theory (DFT) to systematically study the B-site cation ordered structure, along with the preferred oxygen vacancy occupation site in BCN, to better understand the underlying physical mechanisms. First, the B-site ordering is studied by comparing different B-site cation configurations. Then, the preferred $V_{\ddot{O}}$ occupation site is studied in three cases: $V_{\ddot{O}}$ only, coexistence of $V_{\ddot{O}}$ and V''_{Ca}, and coexistence of $V_{\ddot{O}}$ and Y''_{Nb}. We are able to explain both the B-site cation ordering and the $V_{\ddot{O}}$ occupation preference, in terms of ionic bond strength.

4.2 Computational Method

The spin-polarized first principles calculations are performed using a DFT based *ab initio* simulation package, VASP[28]. A supercell containing 12 ABO_3 formula units, which is 2×2×3 times of a single cubic unit cell, is used in this study as the model system. To ensure the accuracy of the calculation, a 6×6×4 k-point mesh and 750 eV kinetic energy cutoff (the hard potential for O is chosen) are used, which leads to an energy convergence within 1 meV/atom and a force convergence within 0.01 eV/Å. Perdew-Burke-Ernzerhof (PBE)[29] exchange-correlation functional with the projector-augmented-wave approach is used. Charge analysis is done by the Bader charge analysis tool[30] (this partition method may lead to ~30% uncertainty in the value of the effective charge, but

qualitatively, the relative trend in one system is reliable). All the supercells involved in this work are fixed at the computational equilibrium stoichiometric BCN lattice constants with all the internal atomic coordinates optimized. In what follows, if not specified, the energy is presented as the relative energy in unit of eV/supercell, with the lowest-energy configuration set as the reference of zero energy.

4.3 Results and Discussion

4.3.1 Strain Energy Associated with B-Site Cation Exchange and Oxygen Vacancy Formation

The optimized lattice constant for the face-center-cubic BCN unit cell is a = 4.184 Å, which agrees with experimental results[11,15,17,21-23]. To check the role played by the difference of ionic radius in the B-site cation ordering and $V_{\ddot{O}}$ formation, we first study the strain energy associated with the changing of the B-site cation ordering. For simplicity, we start from the 1:2 ordered structure along <111> direction as commonly reported in experiments[15], which is schematically shown in Fig. 4.1. Then we exchange one of the Ca atoms with one of its surrounding Nb atoms. As shown in Fig. 4.2(a), there are several possible exchange types, noted as 1-1x, 1-1y, 1-1z, 2-2x, 2-2y, 2-2z, and 2-2z', respectively. To study the strain energy associated with $V_{\ddot{O}}$ formation, we hypothetically remove one oxygen atom from the supercell. The $V_{\ddot{O}}$ concentration is determined to be 1.14×10^{-21} cm^{-3}.

It is found that the strain energy associated with the B-site cation exchange is negligible. The largest stress upon cation exchange is less than 3 kBar, meaning the effective strain energy is less than 0.002 eV. The strain energies in this work are estimated using the linear elasticity assumption according to the formula of $E = \frac{1}{2}\sigma^2 V/B_0$,

where E is strain energy, σ is stress, V is the volume, and B_0 is the bulk modulus. Obviously, the strain energy is far less than the Ca/Nb exchange energy as shown in Table 4.1. This implies that in contrast to some recent suggestion[21,27], the difference in the cation ionic radius plays a negligible role in the B-site cation ordering process. Also, the strain effect due to the $V_{\ddot{O}}$ formation can be neglected. The largest stress upon formation of one $V_{\ddot{O}}$ is less than 10 kBar, meaning the associated strain energy is less than 0.02 eV. This is again several orders of magnitude less than the energy difference between $V_{\ddot{O}}$ occupying different sites, as shown in Tables 4.2, 4.3 and 4.4. Therefore, we conclude that the ionic radius difference is insignificant in determining the B-site cation ordering and the $V_{\ddot{O}}$ site preference.

4.3.2 B-site Cation Ordering in BCN

Starting from the 1:2 fully ordered atomic structure, we exchange one of the Ca atoms with one of its surrounding Nb atoms to study the B-site cation ordering in BCN. As shown in Fig. 4.2(a), there are several possible exchange types, denoted as 1-1x, 1-1y, 1-1z, 2-2x, 2-2y, 2-2z, and 2-2z', respectively. We compare the exchange energies as listed in Table 4.1, where $N_{Ca\text{-}O\text{-}Ca}$, $N_{Nb\text{-}O\text{-}Nb}$, and $N_{Ca\text{-}O\text{-}Nb}$ denote the number of Ca-O-Ca bonds, Nb-O-Nb bonds, and Ca-O-Nb bonds, respectively. The exchange energies listed in Table 4.1 are for stoichiometric BCN; introduction of $V_{\ddot{O}}$ may lower the exchange energies by amount of less than 0.5 eV. Clearly, there is a correlation between the numbers of different bond combination compositions and the exchange energy. The Ca-O-Ca bond plays the primary role; the more NN Ca-O-Ca bonds, the higher the exchange energy. The Nb-O-Nb bond plays the second most important role; the more the NN Nb-O-Nb bonds, the higher the exchange energy for the given number of Ca-O-Ca bonds.

Approximately, we express the total energy of the unit cell as the sum of bond energies as

$$E = N_{Ca\text{-}O\text{-}Ca} \times E_{Ca\text{-}O\text{-}Ca} + N_{Nb\text{-}O\text{-}Nb} \times E_{Nb\text{-}O\text{-}Nb} + N_{Ca\text{-}O\text{-}Nb} \times E_{Ca\text{-}O\text{-}Nb}, \quad (4.2)$$

where $E_{Ca\text{-}O\text{-}Ca}$, $E_{Nb\text{-}O\text{-}Nb}$, and $E_{Ca\text{-}O\text{-}Nb}$ denote the "bond energy" of Ca-O-Ca, Nb-O-Nb, and Ca-O-Nb bond, respectively. Upon each given B-site cation exchange, $N_{B\text{-}O\text{-}B}$ changes to $N'_{B\text{-}O\text{-}B}$ and E changes to E', which gives the exchange energy for the given change process as E'-E. Then, we have the exchange energy as a function of different bond combinations, obtained from a series of DFT calculations, and we can solve a group of equations and extract the relative "bond-energy" contributions to the B-site cation exchange energy from different bond combinations. They are found to be $E_{Ca\text{-}O\text{-}Ca}$=0.708 eV, $E_{Nb\text{-}O\text{-}Nb}$=0.416 eV and $E_{Ca\text{-}O\text{-}Nb}$=0.133 eV, respectively. As shown in Fig. 4.2(b), we see an excellent agreement between the DFT calculated and the model estimated exchange energies based on the extracted B-O-B bond unit contributions to the system energies. We have also calculated the Madelung energy[26,31,32] associated with the cation exchange, using both the formal and effective ionic charge extracted from DFT calculations, as shown in Table 4.1. Qualitatively, the Madelung energies using either formal or effective charges give a reasonable trend in comparison with the DFT results. We have used Bader effective charge for our analysis, which is presently the most widely adopted scheme in DFT calculation. Usually the absolute value of effective charge may vary depending on the different schemes of volume partition used, however, the relative charge difference between different species is reliable. Especially, the effective charge can take into account relative electronegativity difference between different ions; for example, the averaged effective charges of Ca and Ba are calculated to be +1.44, and

+1.57, in accordance with their respective electronegativity of 1.00[33] and 0.89[33] in BCN, although their formal charge is both +2.

We note that the thermal entropy is not accounted for in our results since our calculations are performed under 0 K. Also, due to the system size limitation, the enthalpy of the fully disordered structure cannot be obtained. On the other hand, some experiments showed that near fully ordered structure can only be obtained at high sintering temperatures around 1650 ^{o}C[15,34]. This indicates that the thermal entropy effect is not significant for this system. We can roughly estimate the maximum configurational entropy associated with the disordering among the B-site cation sublattice alone (neglecting other disorders) according to the random solution theory. This configurational entropy is $-Nk_B(x\ln x + (1-x)\ln(1-x)) = 6.6\times10^{-4}$ eV/K, where N is the number of available B-site, k_B is Boltzmann constant, and x is the B site ion composition. At 1000 K, the common working temperature for BCN based SOFCs, the entropic contribution is ~ 0.66 eV. This value is smaller than the lowest B-site exchange energy according to Table 4.1, so that the enthalpy of B-site exchange is more dominant in controlling the B-site cation ordering process. Also, we have calculated the A-B site Ca/Ba mixing energy to be more than 3 eV, indicating it to be an energetically much less favorable process than the B-site cation exchange process.

Also, by assuming the bonding energies do not change appreciably in different phases of oxides under the condition that the elements have the same valence states, we can calculate the formation energies, $E_{Formation} = E(M_xO_y) - xE(M) - yE(O)$, where M denotes Ca/Nb, x/y denotes the compound formula compositions, and pure elements are used as reference. The formation energy for the bulk oxide 2×CaO, Nb_2O_5, and $Ca_2Nb_2O_7$

turns out to be -13 eV, -21 eV, and -36 eV, respectively, which agrees with the formation enthalpies of -1256 KJ/mol, -1899 KJ/mol, and -3347 KJ/mol at 298 K, as reported[35,36] for 2×CaO, Nb_2O_5, and $Ca_2Nb_2O_7$, respectively. The above two sets of data show an increased mixing bonding energy of the Ca-O-Nb bonds over the Ca-O-Ca and Nb-O-Nb bonds, i.e., 1/2(Ca-O-Ca + Nb-O-Nb) < Ca-O-Nb.

We conclude from our above DFT calculations that the B-site cation ordering is determined by the different bond unit compositions. Specifically, the effective B-O-B bond energies determine the cation distribution profile by favoring the mixed bonds of Ca-O-Nb over the Ca-O-Ca and Nb-O-Nb bonds. For example, the 2-2z' exchange induces the smallest exchange energy because it conserves exactly the original bond distribution, while other exchanges increase the number of Ca-O-Ca and Nb-O-Nb bonds. There is a small energy cost associated with the 2-2z' exchange process because it changes the higher order bonds (e.g., Ca-…-Ca interactions) at larger distances (e.g., one Ca-Ca separation decreasing from 7.247 Å to 5.917 Å).

4.3.3 Preferred Oxygen Vacancy Occupation Site

4.3.3.1 Oxygen Vacancy

To study the preferred oxygen vacancy occupation site, we start from an ideal model BCN system that only has $V_{\ddot{O}}$ introduced without other extrinsic defects, to reveal the relative $V_{\ddot{O}}$ formation energy. Although in the real system, average cation charge states has to be lowered to keep charge balance. Another motivation for this study is that this system is very similar to the off stoichiometric BCN18, which is most commonly used in experiments as a proton conducting electrolyte. However, we cannot directly deal with the BCN18 system due to the system size limitation by DFT (DFT can typically only

handle up to several hundreds of atoms), so alternatively, we remove one O atom from the stoichiometric BCN system to mimic the real situation although this setup may create an electronic defect. Based on the main finding of the B-site cation ordering discussed in this section, we analyze the local atomic coordination and structure around the $V_{\ddot{O}}$ formation site, especially focusing on the nearest neighbor (NN) and the next nearest neighbor (NNN) B-site cations, to identify the underlying reasons governing the $V_{\ddot{O}}$ site preference.

The relative energies for different $V_{\ddot{O}}$ sites are listed in Tables 4.2, 4.3, and 4.4. In Table 4.3, NN and NNN denote the first nearest neighbor and the second nearest neighbor of B-cations around the $V_{\ddot{O}}$ site occupying the AO layer, respectively. For the notation of x/y, the former number x denotes the number of Ca atoms and the latter number y denotes the number of Nb atoms, respectively. The same signs apply to Table 4.4 except that the $V_{\ddot{O}}$ occupies the BO_2 layer instead of the AO layer as in Table 4.3; this notation is used throughout this work. The AO and BO_2 plane corresponds to the 2×2 x-y plane in the $2\times2\times3$ supercell used, as schematically shown in Fig. 4.1. Table 4.2 shows the energies when $V_{\ddot{O}}$ occupies the AO plane and BO_2 plane, respectively. Table 4.3 and Table 4.4 show the energies for $V_{\ddot{O}}$ occupying the irreducible B-cation sites in the AO and BO_2 layer, respectively. In addition, Figure 4.3(a) is plotted for better demonstration. Evidently, $V_{\ddot{O}}$ prefers to occupy the BO_2 layers over the AO layers. Also, the relative energies in a certain layer group increases with the increasing number of NNN Ca atoms with the same number of NN Ca atoms. The most preferred $V_{\ddot{O}}$ site is the O site in the BO_2 layer, which has only one NN and one NNN Ca atom.

Our analysis shows that the dominant factor affecting the $V_{\ddot{O}}$ site preference is the

initial effective charge on the removed O ion, based on Bader charge analysis. The absolute values of the effective charges for irreducible O atom sites are shown in Tables 4.3, 4.4 and Figure 4.3(b). One clearly sees that the effective charge on an O ion is mainly determined by its surrounding B cation compositions (we consider its neighboring B-site cations up to the 2nd order, i.e., NN and NNN). Similar to the process where we extracted the B-O-B bond energy, from the charge difference and the difference in the surrounding B cation compositions, we can solve a group of equations and extract the relative contribution to the increase of the effective charge on any O ion. We found the effective charge increase caused by one NN Ca is 0.044 *e* while that caused by one NNN Ca is 0.031 *e*. Generally, with the increasing number of Ca atoms in the NN/NNN layer around the removed O ion, the system energy increases (Fig. 4.3(a)) due to the increase of the initial effective charge on the O ion (Fig. 4.3(b)). This finding is consistent with the electronegativity difference between Ca (1.00)[33] and Nb (1.6)[33] since both of them bond to O.

Also, from Table 4.2, we see that $V_{\ddot{O}}$ is easier to form in the BO_2 layer than in the AO layer. The reason is that the effective charge on the AO layer is positive (~ +1.25 *e*) while it is negative on the BO_2 layer (~ -0.81 *e* for a layer containing one Ca atom and ~ -2.12 *e* for a layer containing two Ca atoms), and the formation of one $V_{\ddot{O}}$ effectively leaves two holes. Therefore, to minimize the magnitude of the effective charge in a certain layer, $V_{\ddot{O}}$ prefers to form in the BO_2 layers. One also sees that the $V_{\ddot{O}}$ occupying a site that does not have Ca as NN (as denoted by 0/2) behaves differently from the $V_{\ddot{O}}$ that has one NN Ca (as denoted by1/1), either in the AO or BO_2 layer. If we consider the bond energy, it seemed the energy of "0/2" would be higher than that of "1/1" because the Nb-O-Nb

bond for the "0/2" site is relative stronger than the Ca-O-Nb bond for the "1/1" site. However, structural relaxation results show that upon $V_{\ddot{O}}$ formation, the NN Nb moves away from the $V_{\ddot{O}}$ while the NN Ca moves closer to the $V_{\ddot{O}}$. Consequently, the Nb-$V_{\ddot{O}}$-Nb distance for the "0/2" site is increased by ~ 0.1 Å, while the Ca-$V_{\ddot{O}}$-Nb distance for the "1/1" sites is almost unchanged, so that the resulting Nb-$V_{\ddot{O}}$-Nb unit energy becomes lower. The same reasoning can be applied to the $V_{\ddot{O}}$ occupying BO_2 plane, except one has to also consider the large charge difference between the two types of BO_2 planes. The O ion with "3/5" NNN configuration exists only in the most negative BO_2 plane (~ -2.12 e), so that the $V_{\ddot{O}}$ formation tends to primarily minimize the effective charge of the BO_2 plane. As shown in Table 4.4, the $V_{\ddot{O}}$ formation energy of the NN 0/2 – NNN 4/4 is higher than that of the NN 1/1 – NNN 3/5, because the former configuration removes an O ion from a BO_2 plane having a much smaller effective charge (-0.81e) than the latter (-2.12e). In addition, a stronger Nb-O-Nb bond is broken in the former configuration.

To better understand the $V_{\ddot{O}}$ formation, we further analyzed the charge redistribution and ionic relaxation upon the $V_{\ddot{O}}$ formation in the most preferred site. As shown in Fig. 4.4, we find that charge redistribution only happens on the oxygen atoms in the Ca-$V_{\ddot{O}}$-Ca plane. The O atoms that are NN to Ca receive the most extra charge, especially for the O atom between the $V_{\ddot{O}}$ and NNN Ca atoms. The reason is that the O ion, which is mostly surrounded by Ca atoms, prefers to be in a higher charge state (as we discussed previously). In addition, ionic relaxation mainly happens on those oxygen atoms in the same Ca-$V_{\ddot{O}}$-Ca plane (ionic displacements range from 0.1 Å to 0.4 Å). This amounts to 75.5% of total strain relaxation energy, which is calculated as the sum of the second power of all the atomic displacements.

In summary, we reveal that the dominating underlying driving force for the preferred $V_{\ddot{O}}$ site is the initial effective charge on the removed O ion. The breaking of the B-O-B bond, as well as the decrease of the effective charge of AO/BO_2 planes, contributes also to the relative system energies.

4.3.3.2 Coexistence of Oxygen Vacancy and Ca Vacancy

Based on the finding in Section 4.3.3.1, we consider next the situation where $V_{\ddot{O}}$ and V''_{Ca} coexist which satisfies the charge balance consideration. Because it is impractical to examine all the possible configurations of $V_{\ddot{O}}$-V''_{Ca} complexes, we will consider only the limiting cases where we place the V''_{Ca} next to the most stable $V_{\ddot{O}}$ sites as determined in Section 4.3.3.1. The relative energies for V''_{Ca} occupying different sites are shown in Table 4.3, where d($V_{\ddot{O}}$-V''_{Ca}) denotes the separation distance between $V_{\ddot{O}}$ and V''_{Ca}. The V''_{Ca} is found to prefer to occupy the NN sites to $V_{\ddot{O}}$ due to two reasons: (1) small d($V_{\ddot{O}}$-V''_{Ca}) to minimize the electrostatic energy; and (2) removal of one relatively weaker Ca-O bond unit. Generally, the larger the d($V_{\ddot{O}}$-V''_{Ca}), the higher the system energy. However, there is one exception that for d($V_{\ddot{O}}$-V''_{Ca}) equals to 5.916 Å vs. 6.276 Å, the system energy is found lower at larger distance of 6.276 Å. This can be understood from the effective charge analysis we discussed in Section 4.3.3.1. Specifically, for the case of d($V_{\ddot{O}}$-V''_{Ca}) = 5.916 Å, the V''_{Ca} is formed by removing a Ca atom from the Ca-$V_{\ddot{O}}$-Ca plane but away from $V_{\ddot{O}}$, so that those O atoms being NN to the removed Ca acquire a higher effective charge due to the $V_{\ddot{O}}$ induced charge redistribution within this plane. In contrast, for the case of d($V_{\ddot{O}}$-V''_{Ca}) = 6.276 Å, the V''_{Ca} is formed by removing a Ca atom outside of the Ca-$V_{\ddot{O}}$-Ca plane without charge redistribution, so that those O atoms being NN to the removed Ca have a lower effective charge. Consequently, the energy cost to form the

d($V_{\ddot{O}}$-V_{Ca}'') = 5.916 Å configuration is higher because it breaks stronger B-O-B bonds to form the V_{Ca}'', even though the resulting $V_{\ddot{O}}$-V_{Ca}'' interaction energy is lower with a shorter distance. In the other three cases, the final $V_{\ddot{O}}$ - V_{Ca}'' interaction energy difference dominates because of a much larger difference in distance, so that the initial effective charge difference of O atoms NN to the removed Ca is not important.

4.3.3.3 Coexistence of Oxygen Vacancy and Y Replacing Nb Defect

Next, we discuss the extrinsic defect Y_{Nb}'' in the presence of $V_{\ddot{O}}$, which is widely studied in experiments. Similar to Section 4.3.3.2, because it is impractical to examine all the possible configurations of $V_{\ddot{O}}$-Y_{Nb}'' complexes, we will consider only the limiting cases where we place the Y_{Nb}'' next to the most stable $V_{\ddot{O}}$ sites as determined in Section 4.3.3.1. The relative system energies for Y occupying different Nb site are shown in Fig. 4.5. It is shown that the most preferred occupation site for Y is the NN to $V_{\ddot{O}}$. Further, for the same NN cation configurations, the system energy generally increases with the increasing d($V_{\ddot{O}}$-Y_{Nb}'') distance. For the same d($V_{\ddot{O}}$-Y_{Nb}'') distance, the system energies increase with the increasing number of Ca atoms in the NN layer. Similarly, two factors that determine the Y position can be recognized: (1) Y prefers to stay close to $V_{\ddot{O}}$ to minimize electrostatic energy; and (2) Y prefers to replace the Nb which is surrounded by less Ca (more Ca induces larger effective charge on O, stronger B-O-B bonds). The net balance between these two factors determines the Y occupation site.

4.4 Conclusions

Using density functional theory calculations, we have studied the underlying driving forces for the B-site cation ordering and the preferred oxygen vacancy occupation site in

BCN. We found that the effect of ionic radius difference is negligible, different from what is being suggested by some recent literature[21,27]. On the other hand, we found ionic bond strength plays the dominant role, consistent with previous electrostatic energy analyses[25,26]. The B-O-B bond strength determines the B-site cation ordering, by favoring the low-energy configuration with the maximized number of mixed Ca-O-Nb bonds over the combination of Ca-O-Ca and Nb-O-Nb bonds. The formation of the oxygen vacancy is preferred to remove the O ion having the lower effective charge as well as breaking the weaker B-O-B bond. Our findings give a better understanding of the atomic processes of cation exchange and oxygen vacancy site preference in BCN, based on ionic bond strength. We believe the physical mechanisms we uncover here from first-principles calculations might be generally applied to similar complex $A_3B'B''_2O_9$ perovskites.

4.5 Acknowledgements

We acknowledge the financial support from DOE EFRC Grant Number DE-SC0001061 as a flow through from the University of South Carolina. Also, we thank DOE-NERSC and CHPC at the University of Utah for providing computing resources.

4.6 References

[1] S.C. Singhal, *Solid State Ionics* **135**, 305 (2000).

[2] H. Ding, A.V. Virkar, M. Liu, F. Liu, *Phys. Chem. Chem. Phys.* **15**, 489 (2013).

[3] S.C. Singhal, *Solid State Ionics* **152-153**, 405 (2002).

[4] B.C. Steele, A. Heinzel, *Nature* **414**, 345 (2001).

[5] H. Ding, A.V. Virkar, F. Liu, *Solid State Ionics* **215**, 16 (2012).

[6] A.S. Nowick, Y. Du, *Solid State Ionics* **77**, 137 (1995).

[7] A.S. Nowick, Y. Du, K.C. Liang, *Solid State Ionics* **125**, 303 (1999).

[8] W. Wang, A.V. Virkar, *J. Electrochem. Soc.* **151**, A1565 (2004).

[9] W. Wang, A.V. Virkar, *J. Electrochem. Soc.* **150**, A92 (2003).

[10] S.S. Bhella, V. Thangadurai, *J. Power Sources* **186**, 311 (2009).

[11] S.S. Bhella, V. Thangadurai, *J. Electrochem. Soc.* **156**, B634 (2009).

[12] E. Fabbri, D. Pergolesi, E. traversa, *Chem. Soc. Rev.* **39**, 4355 (2010).

[13] E. Fabbri, L. Bi, D. Pergolesi, E. traversa, *Adv. Mater.* **24**, 195 (2012).

[14] S. Wang, L. Zhang, Z. Yang, L. Zhang, S. Fang, K. Brinkman, F. Chen, *J. Power Sources* **215**, 221 (2012).

[15] J. Rodrigues, E. Moreira, D. Bezerra, A. Maciel, C. Paschoal, *Mater. Res. Bull.* **48**, 3298 (2013).

[16] T. Schober, J. Friedrich, *Solid State Ionics* **136-137**, 161 (2000).

[17] K. Oikawa, T. Kamiyama, S. Ikeda, T. Shishido, S. Yamaguchi, *Solid State Ionics* **154-155**, 641 (2002).

[18] K.C. Liang, Y. Du, A.S. Nowick, *Solid State Ionics* **69**, 117 (1994).

[19] M. Pionke, T. Mono, W. Schweika, T. Springer, H. Schober, *Solid State Ionics* **97**, 497 (1997).

[20] B. Grob, S. marion, K. Lind, D. Grambole, F. Herrmann, R. Hempelmann, *Solid State Ionics* **107**, 107 (1999).

[21] J. Deng, J. Chen, R. Yu, G. Liu, X. Xing, *J. Alloy Compd.* **472**, 502 (2009).

[22] T. Mono, T. Shober, *Solid State Ionics* **91**, 155 (1996).

[23] M. Yokosuka, *Jpn. J. Appl. Phys.* **32**, 4578 (1993).

[24] Y. Du, A.S. Nowick, *J. Am. Ceram. Soc.* **78**, 3033 (1995).

[25] L. Bellaiche, D. Vanderbilt, *Phys. Rev. Lett.* **81**, 1318 (1998).

[26] S. Bhide, A. Virkar, *J. Electrochem. Soc.* **146**, 4386 (1999).

[27] Q. Zhou, B.J. Kennedy, J.A. Kimpton, *J. Solid State Chem.* **184**, 729 (2011).

[28] G. Kresse, J. Hafner, *Phys. Rev. B* **54**, 11169 (1996).

[29] J. P. Perdew, K. Burke, M. Ernzerhof, *Phys. Rev. Lett.* **77**, 3865 (1996).

[30] W. Tang, E. Sanville, G. Henkelman, *J. Phys.: Condens. Matter* **21**, 084204 (2009).

[31] T. Nakamura, *J. Solid State Chem.* **38**, 229 (1981).

[32] N. Kimizuka, A. Yamamoto, H. Ohashi, T. Sugihara, T. Sekine, *J. Solid State Chem.* **49**, 65 (1983).

[33] L. Pauling, *The Nature of the Chemical Bond*, Cornell Univ. Press, USA, **3rd** ed. (1960).

[34] J. Deng, J. Chen, R. Yu, G. Liu, X. Xing, S. Han, Y. Liu, D. Chen, L. He, *Solid State Ionics* **11**, 170 (2009).

[35] I. Barin, *Thermochemical data of Pure Substances*, VCH Publishers (1989).

[36] J. Leitner, K. Ruzicka, D. Sedmidubsky, P. Svoboda, *J. Therm. Anal. Calorim.* **95**, 397 (2009).

Table 4.1 The relative system energies (exchange energies) upon Ca/Nb exchange. The first row denotes the exchange types: "Initial" denotes the 1:2 ordered structure, while the others denote the different exchanged structures as shown in Fig. 4.2(a). E_M denotes the calculated Madelung energy from the effective ionic charge extracted from DFT calculations, while the values in the parentheses are obtained from formal empirical charge Madelung energy calculations. "$N_{B\text{-}O\text{-}B}$" denotes the number of B-O-B bond units.

Types	Initial	1-1x/y	1-1z	2-2x/y	2-2z	2-2z'
ΔE (eV)	0	2.868	1.747	1.444	4.590	0.797
E_M (eV)	0	18 (33)	14 (37)	6 (29)	19 (47)	13 (37)
$N_{Ca\text{-}O\text{-}Ca}$	0	4	3	3	6	0
$N_{Nb\text{-}O\text{-}Nb}$	12	14	13	11	14	12
$N_{Ca\text{-}O\text{-}Nb}$	24	18	20	22	16	24

Table 4.2 The lowest relative system energies for $V_{\ddot{O}}$ occupying AO and BO_2 layers.

Atomic layer	AO layer	BO_2 layer
ΔE (eV)	0.394	0.000

Table 4.3 The relative system energies for $V_{\ddot{O}}$ occupying AO layers. The first row shows the number of Ca/Nb in the NN layer around the $V_{\ddot{O}}$, and the second row shows the number of Ca/Nb in the NNN layer around the $V_{\ddot{O}}$. The third row shows the initial effective charges on the removed $V_{\ddot{O}}$.

AO/NN	0/2	1/1		
NNN	4/4	0/8	2/6	4/4
$q_{effective}$ (e)	1.273	1.192	1.263	1.317
ΔE (eV)	0.394	0.439	0.438	0.916

Table 4.4 The relative system energies for $V_{\ddot{O}}$ occupying BO_2 layers. The first row shows the number of Ca/Nb in the NN layer around the $V_{\ddot{O}}$, and the second row shows the number of Ca/Nb in the NNN layer around the $V_{\ddot{O}}$. The third row shows the initial effective charges on the removed $V_{\ddot{O}}$.

BO_2/NN	0/2	1/1	
NNN	4/4	1/7	3/5
$q_{effective}$ (e)	1.275	1.232	1.294
ΔE (eV)	0.190	0.000	0.164

Table 4.5 The relative energies for V_{Ca}'' occupying different sites with different separation to $V_{\ddot{O}}$.

d($V_{\ddot{O}}$-V_{Ca}'')	2.092 Å	5.916 Å	6.276 Å	7.247 Å
ΔE (eV)	0.000	4.843	4.184	5.320

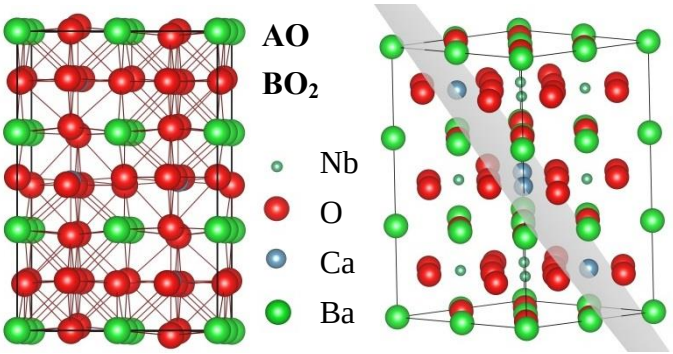

(a) (b)

Fig. 4.1 The crystal structure of BCN. (a) Demonstration of the BCN crystal structure; (b) The Ca atom layer in the 1:2 ordering along the <111> direction. Large Lime balls denote Ba, sky-blue balls denote Ca, small green balls denote Nb, and red balls denote O. "AO" denotes BaO layer and "BO_2" denotes (Ca/Nb)O_2 layer.

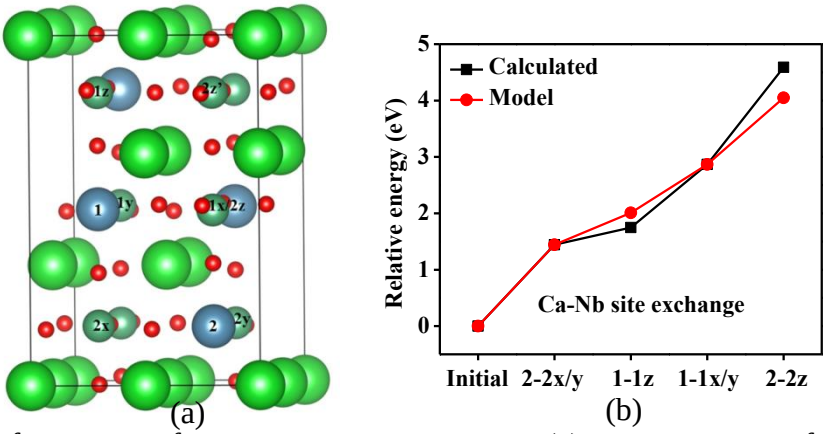

(a) (b)

Fig. 4.2 Effect of atomic configuration on system energy. (a) Demonstration of the Ca/Nb exchange types, where 1 and 2 are Ca atoms, 1x, 1y, 1z, 2x, 2y, 2z, and 2z' are the exchange process involved Nb atoms. The colors represent the same atom types as in Fig. 4.1, but the ionic radii are changed from ionic radius to atomic radius for better demo. (b) Relative system energy (exchange energy) upon cation exchange, black square line denotes the calculated results, and red circle line denotes the modeling derived values. "Initial" denotes the 1:2 ordered structure, while the others denote the different exchanged structures.

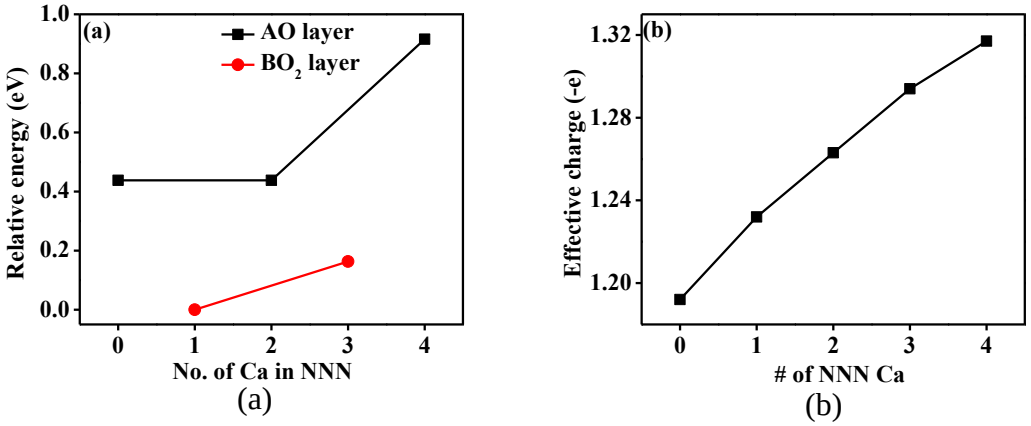

Fig. 4.3 Relation between effective charge and relative $V_{\ddot{O}}$ formation energy. (a) Relative energies for oxygen vacancy formation occupation sites vs. the number of Ca atoms in the NNN layer. Black squared line denotes the $V_{\ddot{O}}$ formation in AO layers, and red circled line denotes the $V_{\ddot{O}}$ formation in BO_2 layers. (b) O ion effective charge vs. the number of Ca atoms in the NNN layer. The number of Ca atoms in the NN layer is fixed at 1.

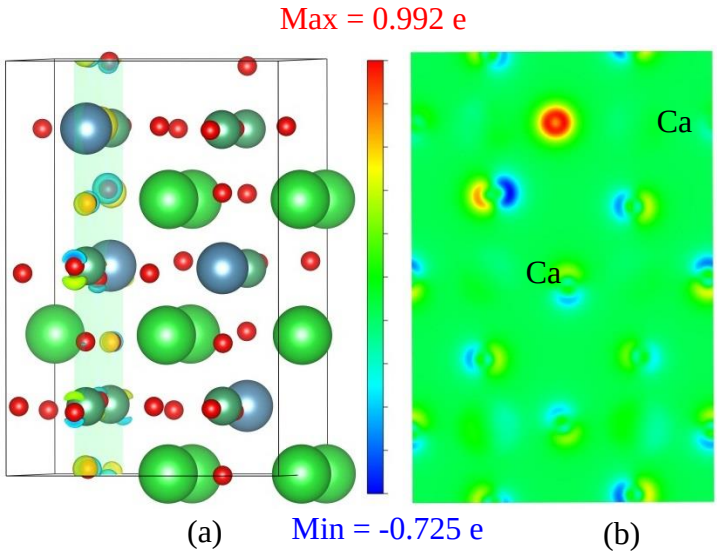

Fig. 4.4 Charge density difference plots upon $V_{\ddot{O}}$ formation in BCN. (a) 3D view. (b) 2D view at the atomic plane marked in Fig. 4.4(a).

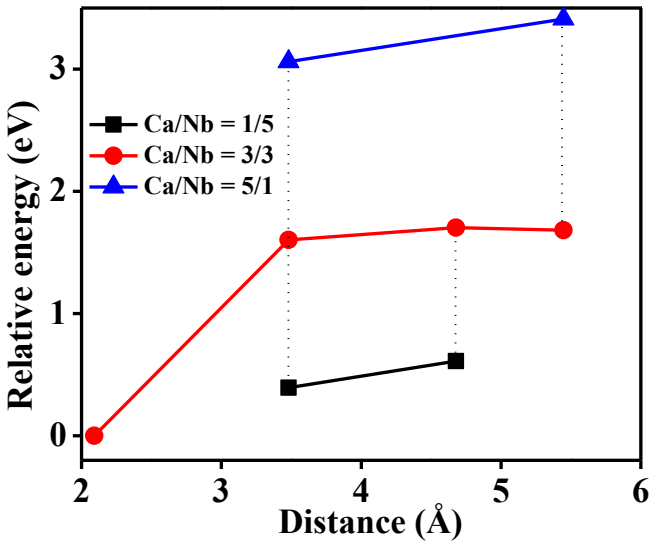

Fig. 4.5 Relative energies for Y''_{Nb} formation occupation sites vs. d($V_{\ddot{O}}$-Y''_{Nb}) distance. The numbers in "Ca/Nb= *x*/*y*" denote there are x Ca atoms and y Nb atoms in the NN layer around the Y''_{Nb}. Dashed lines denotes the same d($V_{\ddot{O}}$-Y''_{Nb}) distance but with different NN layer cation configurations.

CHAPTER 5

CONCLUSIONS

To summarize, in this dissertation, we have employed DFT calculations to systematically investigate the microscopic processes related to the doping-induced defects occurring in the materials useful for SOFC system. We focused on three topics: the defect configuration in oxygen conducting electrolyte YSZ; the defect modified Sr surface segregation on the cathode made of LSCF; and the B-site cation ordering and defect of oxygen vacancy site preference in the proton conducting electrolyte BCN. Through these works, we demonstrate that first-principles atomistic level calculations can be used as an effective tool to reveal the fundamental physical principles that underlie some of the intricate processes taking place in the operation of SOFCs, and predict properties of electrolytes and cathodes in SOFCs and other electrochemical energy conversion/storage devices, which may guide the future experimental design.

We note that the three topics studied by first-principles calculations in this dissertation are thermodynamic or energetics studies, including the defect interaction energy in oxygen conducting electrolyte YSZ, the A-site cation exchange energy in the cathode materials of LSCF, and the B-site cation ordering energy in the proton conducting electrolyte BCN. However, first-principles calculations can also be used for studying kinetics, i.e., energy barriers of kinetic processes, at the atomistic level.

Therefore, future works may be directed towards this area of research, to address important kinetic issues associated with the microscopic processes in the materials used for SOFCs. These types of first-principles calculations are usually more computationally demanding, such as calculations of the reaction, diffusion, and transport processes. Moreover, to take full advantage of computational simulation and modeling, multiscale methods can be employed. Using the first-principles calculation results as a benchmark, empirical force fields can be developed to carry out molecular dynamics simulations to compute much larger atomistic systems and for much longer time scales. The output of the atomistic simulations can in turn provide the critical microscopic input parameters, both the thermodynamic and kinetic parameters, for continuum models and field equations.